

1 **The sensitivity of Southeast Pacific heat distribution to local and remote**
2 **changes in ocean properties**

3 Daniel C. Jones*, Emma Boland, Andrew J.S. Meijers

4 *British Antarctic Survey, NERC, UKRI, Cambridge, UK*

5 Gael Forget

6 *Massachusetts Institute of Technology, Cambridge, MA, USA*

7 Simon Josey

8 *National Oceanography Centre, Southampton, UK*

9 Jean-Baptiste Sallee

10 *L'Ocean, CNRS, Paris, France*

11 Emily Shuckburgh

12 *University of Cambridge, UK*

13 **Corresponding author address: D.C. Jones, British Antarctic Survey, NERC, UKRI, Cambridge,*

14 **UK.**

15 **E-mail: dannes@bas.ac.uk**

ABSTRACT

16 The Southern Ocean features ventilation pathways that transport surface wa-
17 ters into the subsurface thermocline on timescales of decades to centuries,
18 sequestering anomalies of heat and carbon away from the atmosphere and
19 thereby regulating the rate of surface warming. Despite its importance for
20 climate sensitivity, the factors that control the distribution of heat along these
21 pathways are not well understood. In this study, we use an observationally-
22 constrained, physically consistent global ocean model to examine the sensi-
23 tivity of heat distribution in the recently ventilated subsurface Pacific (RVP)
24 sector of the Southern Ocean to changes in ocean temperature and salinity.
25 First, we define the RVP using numerical passive tracer release experiments
26 that highlight the ventilation pathways. Next, we use an ensemble of adjoint
27 sensitivity experiments to quantify the sensitivity of the RVP heat content to
28 changes in ocean temperature and salinity. In terms of sensitivities to surface
29 ocean properties, we find that RVP heat content is most sensitive to anomalies
30 along the Antarctic Circumpolar Current (ACC), upstream of the subduction
31 hotspots. In terms of sensitivities to subsurface ocean properties, we find that
32 RVP heat content is most sensitive to basin-scale changes in the subtropi-
33 cal Pacific Ocean, around the same latitudes as the RVP. Despite the localized
34 nature of mode water subduction hotspots, changes in basin-scale density gra-
35 dients are an important controlling factor on heat distribution in the Southeast
36 Pacific.

37 **1. Introduction**

38 The Southern Ocean (SO) is an important region for the uptake, storage, and transport of heat and
39 carbon; SO upwelling brings up water that has not seen the surface for centuries or even millennia
40 and is thus far out of equilibrium with surface temperature and atmospheric carbon (Sabine et al.
41 2004; Sarmiento et al. 2004; Lenton and Matear 2007; Ito et al. 2010; Talley 2013; Roemmich et al.
42 2015; Armour et al. 2016). Over the period 1861-2005, the SO, defined as the ocean south of 30°S,
43 is estimated to account for $43\% \pm 3\%$ of anthropogenic carbon dioxide uptake and $75\% \pm 22\%$ of
44 heat uptake, despite only occupying 30% of global surface ocean area (Frölicher et al. 2015). The
45 SO's ability to absorb and transport this disproportionately high fraction of heat and carbon comes
46 in part from a balance between powerful overlying westerly winds, strong buoyancy fluxes, and
47 internal dynamics that maintains steeply tilted surfaces of constant density and localized pools
48 of weakly stratified water (Russell et al. 2006). These pools of weakly stratified water, referred
49 to collectively as Subantarctic Mode Water (SAMW), are refreshed by localized wintertime deep
50 convection that occurs just north of the Antarctic Circumpolar Current (ACC) (Speer et al. 2000;
51 Hanawa and Talley 2001; Lumpkin and Speer 2007; Talley 2008; Herraiz-Borreguero and Rintoul
52 2011; Speer and Forget 2013). The processes of lateral induction, eddy-induced transport, and
53 advection via the mean flow subduct the SAMW into the subsurface ocean at a rate that varies
54 across interannual and decadal timescales (Karsten and Marshall 2002; Sallée et al. 2010b; Sallée
55 and Rintoul 2011; Sallée et al. 2012; Liu and Huang 2012). Together with the denser and relatively
56 fresher Antarctic Intermediate Water (AAIW), SAMW ventilates the subtropical thermocline on
57 timescales of decades to centuries (Iudicone et al. 2007; Sallée et al. 2010a; Cerovecki et al. 2013;
58 Jones et al. 2016). Here, ventilation refers to the broad set of processes by which atmospheric
59 and surface ocean properties are able to affect subsurface ocean properties. Ventilation is driven

60 in part by the formation, subduction, and destruction of water masses and can be considered a
61 consequence of the ocean's global overturning circulation (Marshall and Speer 2012; Cerovečki
62 and Mazloff 2015).

63 SAMW and AAIW both display complex patterns of decadal variability. In the Western Pacific,
64 decadal-scale surface warming and/or freshening at high-latitude SAMW and AAIW subduction
65 sites can lead to cooling and freshening along isopycnals in the subsurface (Johnson and Orsi
66 1997). Decadal trends in SAMW temperature and salinity display complex spatial variability; in
67 recent decades, both the SAMW and AAIW have become warmer and saltier in the South Atlantic
68 but cooler and fresher in the South Atlantic (Katsumata and Fukasawa 2011). The AAIW core (its
69 salinity minimum) has warmed and shoaled overall, with small salinity trends whose sign varies
70 by region (Schmidtko and Johnson 2012). Decadal trends of SAMW and AAIW properties are
71 consistent with an amplification of the global hydrological cycle and broad-scale surface warming
72 (Helm et al. 2010; Durack and Wijffels 2010). The spatial and temporal complexity of these
73 SAMW and AAIW trends suggests that we will need a full four-dimensional description of the
74 sensitivity of ocean structure in order to make robust projections of potential future ocean states.

75 Regional differences in subduction, ventilation, and the properties of the ventilated subsurface
76 can impact (i.) the sequestration of anthropogenic heat and carbon into the subsurface thermocline
77 and (ii.) the supply of nutrients to low latitudes via the overturning circulation (Sarmiento et al.
78 2004; Sabine et al. 2004; Khatiwala et al. 2009; Ito et al. 2010; Roemmich et al. 2015). The
79 regionally specific nature of subduction and ventilation, and how those localized characteristics
80 affect the distribution of heat, carbon, and nutrients in the ocean, is an active area of oceanographic
81 study (Cerovecki et al. 2013; Jones et al. 2016). Despite these efforts, we still have relatively little
82 knowledge on how regional variations in ocean state variables (e.g. temperature, salinity) and
83 surface forcing can ultimately impact the properties of the ventilated subsurface. Advancements in

84 this area may be especially helpful for improving projections of future ocean states, as changes in
85 the Southern Ocean forcing-subduction-ventilation mechanism are expected to have a considerable
86 impact on future climate (Cessi and Otheguy 2003; Downes et al. 2009; Lovenduski and Ito 2009;
87 Morrison et al. 2011; Sallée et al. 2012).

88 In order to quantify how regional variations in ocean state variables may affect the heat distribu-
89 tion in the ventilated subsurface ocean, we perform a set of adjoint sensitivity experiments using
90 an observationally-constrained, physically consistent state estimate. First, we identify the recently
91 ventilated subsurface ocean using a combination of physical state variables (e.g. potential vor-
92 ticity, density, mixed layer depth) and numerical passive tracer distributions that track ventilation
93 pathways from the surface into the subsurface. Our method for identifying the recently ventilated
94 subsurface treats ventilation as a general process that may affect many different water masses, in
95 contrast to approaches that consider one particular water mass (e.g. SAMW). We focus our atten-
96 tion on the Eastern Pacific because it features an especially efficient export pathway of water from
97 the surface ocean into the subsurface thermocline, as measured by numerical passive tracer exper-
98 iments (Jones et al. 2016). For convenience, we refer to the recently ventilated subsurface Eastern
99 Pacific as the RVP and the heat content of the RVP as RVPh. Although there is overlap between
100 the two, we note that the RVP is more general than the region occupied by SAMW or any other
101 particular water mass. Once we have identified the RVP, we perform a set of adjoint sensitivity
102 experiments using, for consistency, the same numerical model setup that we used for the passive
103 tracer experiments. Our adjoint model produces linear, time-evolving sensitivity maps, allowing
104 us to identify locations and timescales where hypothetical anomalies could potentially impact the
105 heat distribution in the ventilated subsurface, as revealed by the heat content of the fixed-volume
106 RVP. Although we do not use this framework here, the sensitivity fields can roughly be interpreted
107 as optimal linear perturbations, i.e. perturbations with the largest possible impact on RVPh, within

108 the linear framework of the adjoint model (see a related but not identical example in Sévellec and
109 Fedorov (2015)).

110 This paper is structured as follows: in section 2, we describe the ECCOv4 model setup, the
111 design of our numerical tracer release experiments, and the design of our adjoint sensitivity ex-
112 periments. In section 3, we examine the results of the tracer experiments in order to define the
113 RVP, which is the control volume for our adjoint sensitivity experiments. In section 4, we examine
114 the time-evolving sensitivities of RVP_h to changes in temperature and salinity, decomposed into
115 changes at constant density (i.e. kinematic sensitivities) and changes with varying density (i.e.
116 dynamic sensitivities). In section 5, we discuss factors that should be considered when comparing
117 our results with other studies. Finally, in section 6, we summarize our results and conclusions.

118 **2. Methods**

119 In this section, we describe the observationally-constrained global ocean model setup (subsec-
120 tion a), the design of our numerical passive tracer experiments used to define the RVP (subsection
121 b), and the design of our adjoint sensitivity experiments (subsection c).

122 *a. Global ocean model setup*

123 We use the modelling setup associated with ECCOv4 (release 2, hereafter ECCOv4-r2 or just
124 ECCOv4). ECCOv4 is a *state estimate*, meaning that it has been adjusted to minimize the mis-
125 fits between the model state and a suite of observations from various sources over the time period
126 1992-2011 (e.g. Argo float temperature and salinity profiles, ship hydrography, satellite altimetry).
127 The model’s initial conditions, surface forcing fields, and mixing parameters were iteratively ad-
128 justed in order to reduce model-data misfit. Because no artificial sources or sinks of heat were used
129 in the ocean subsurface, ECCOv4 features closed budgets of heat, salt, and volume. The model

130 setup is available for download on GitHub.com (<https://github.com/gaelforget/ECCOv4>) as
131 an instance of the open source MIT general circulation model (MITgcm, <http://mitgcm.org/>,
132 also available on GitHub). We briefly describe the relevant features of the ECCOv4 setup below;
133 a more thorough description is available in Forget et al. (2015a) and references therein.

134 ECCOv4 is a global ocean model that uses a Lat-Lon-Cap (LLC) grid. Its horizontal grid spac-
135 ing ranges from around 40-50 km at high latitudes up to roughly 110 km at the equator. It features
136 parameterized diffusion, including both diapycnal and isopycnal components, simple convective
137 adjustment, and the Gaspar-Gregoris-Lefevre (GGL) mixed layer turbulence closure scheme (Gas-
138 par et al. 1990). To represent the along-isopycnal effect of unresolved eddies, Forget et al. (2015a)
139 used a bolus transport parameterization (Gent and McWilliams 1990, hereafter GM). Although
140 the horizontal resolution of ECCOv4 is relatively coarse (roughly 1°), its mixing properties are in
141 good agreement with observations, as indicated by a comparison of simulated ECCOv4 oxygen
142 distribution and World Ocean Atlas 2013 (Forget et al. 2015b, Figure 4). This agreement is thanks
143 in part to the use of optimized, spatially-varying turbulent transport coefficients. ECCOv4 features
144 fully interactive dynamic sea ice, so that buoyancy and mass fluxes at the sea surface are calculated
145 based on the thermodynamic balance of Losch et al. (2010). Open ocean rain, evaporation, and
146 runoff simply carry (advect through the free surface) the local SST and a salinity value of zero, and
147 runoff is provided by a monthly climatology (Fekete et al. 2002). ECCOv4 calculates buoyancy,
148 radiative, and mass fluxes using the bulk formulae of Large and Yeager (2009) with 6-hourly ERA-
149 Interim re-analysis fields (Dee et al. 2011) as a “first guess” for the forcing fields. Specifically,
150 we use wind stress, 2 m air temperature, 2 m specific humidity, wind speed, downward longwave
151 radiation, and downward shortwave radiation as model inputs. These atmospheric state fields have
152 been iteratively adjusted by the state estimation process in order to minimize model-data misfits.
153 The ECCOv4-r2 setup that we use here does *not* use surface salinity restoring. For additional val-

154 idation information, see Forget et al. (2015a). For calculations relevant to mode water formation
155 and distribution in ECCOv4, see Speer and Forget (2013).

156 *b. Design of the numerical passive tracer release experiments*

157 Generally, on a selected timescale (e.g. 1 year, 10 years), we can consider the volume of the
158 ocean that has been affected by near-surface properties (e.g. the temperature and salinity charac-
159 teristics of the mode water formation regions) as having been ventilated via advection, diffusion,
160 and mixing. In terms of an operational definition, the ventilated subsurface ocean can be identified
161 using physical state variables, tracer distributions, or a combination of the two. Luyten et al. (1983)
162 showed that, in a simple, inviscid, analytical model, pathways of potential vorticity (PV) can be
163 used to separate the ventilated thermocline from the unventilated thermocline and also to separate
164 regions of weak stratification from regions of strong stratification. This result helps justify the
165 use of potential vorticity as a “dynamical tracer” that indicates thermocline ventilation pathways.
166 Alternatively, one can derive ventilation pathways using the observed distributions of tracers such
167 as tritium, helium-3 and chlorofluorocarbons, which are carried into the subsurface by both advec-
168 tion along ventilation pathways and by isopycnal and diapycnal mixing (Musgrave 1990; Speer
169 and Tziperman 1992; Primeau and Holzer 2006). In the subsurface, diapycnal mixing contributes
170 to the erosion of water masses by homogenizing their properties across density surfaces (Tross-
171 man et al. 2012). In combination with PV and tracer considerations, the ventilated subsurface is
172 generally considered to be located below the mixed layer, isolated from immediate contact with
173 the surface. In this study, we use a combination of physical state variables (e.g. PV, mixed layer
174 depth, density) and numerical passive tracer release experiments to identify the recently ventilated
175 subsurface ocean in ECCOv4-r2, described in detail below.

176 First, we use stratification (PV) and mixed layer depth (MLD) to identify the Southern Ocean re-
177 gions that tend to ventilate the subsurface thermocline (Figure 1). We calculate $PV = f\rho_0^{-1}d\rho/dz$,
178 where $f = 2\Omega\sin(\phi)$ is the Coriolis parameter and ρ_0 is the reference density, and we calculate
179 mixed layer depth using a criteria based on the density change associated with a temperature vari-
180 ation of $\Delta T = 0.8^\circ\text{C}$ (Kara et al. 2000). For each year between 1996 and 2001, we calculate the
181 June-July-August (JJA) mean PV and both the JJA mean and annual maximum MLD, and we use
182 these values with a set of criteria to construct a “mixed layer mask” for that year. Specifically, for
183 a grid cell to be included in the mixed layer mask for a given year, it must:

- 184 1. be within the annual maximum mixed layer and
- 185 2. be at a latitude and longitude where one or both of the following conditions are satisfied:
 - 186 (a) the JJA mean $|PV|$ at the base of the JJA mean mixed layer must be less than $10^{-10.5}$
187 1/ms, or
 - 188 (b) the JJA mean mixed layer must be greater than 300 m.

189 These relatively weak conditions ensure that we target likely ventilation pathways without being
190 overly prescriptive.

191 We perform six different tracer release experiments (one for each starting year between 1996 and
192 2001). For each experiment, we initialize passive tracer within the corresponding year’s mixed
193 layer mask on 1 January; our method of initializing tracer above the maximum mixed layer for
194 the release year ensures that variation associated with seasonal release timings are minimal. We
195 integrate the tracer equations in “online” mode for 10 years, i.e. we explicitly solve the momentum,
196 buoyancy, and tracer equations at the same time. Note that although the bulk of the tracer used to
197 define the RVP originates in the Pacific, a smaller fraction also comes from the Indian sector. The
198 10-year timescale of the experiments allows a large fraction of weakly stratified water to subduct

199 into the subsurface (Jones et al. 2016), and using a 10-year timescale also allows us to carry out a
200 suite of passive tracer and adjoint sensitivity runs within the 20-year observationally-constrained
201 time period of ECCOv4. We then use the annual mean tracer distribution after 10 years of model
202 integration to map out the ventilation pathways. See section 3 for more details and results.

203 *c. Design of the adjoint sensitivity experiments*

204 An adjoint model is a tool for sensitivity analysis; all other applications derive from there (Errico
205 1997). Adjoint methods can be used to construct state estimates (e.g. the ECCOv4 state estimate
206 used in this paper) via the iterative optimization of model initial conditions, model parameters,
207 and surface forcing (collectively called the “controls”), guided by *gradients* or *sensitivities* that
208 are calculated by an adjoint model. In such applications, the sensitivities indicate how one needs
209 to adjust the controls in order to reduce the *cost function*, which is a measure of model-data misfit
210 over the duration of the model run. This method enables objective, physically consistent, and
211 efficient model optimization that would otherwise require considerable ad-hoc parameter tuning
212 and/or the introduction of artificial sources or sinks of heat and salt into the subsurface.

213 More generally, adjoint methods also enable us to carry out efficient and comprehensive sensi-
214 tivity studies, such as the one presented in this manuscript. In a traditional “forward” perturbation
215 experiment, the experimenter introduces a perturbation into the model (e.g. a change in the initial
216 temperature pattern) and examines the effect on some quantity of interest (e.g. RVPh). Using this
217 method, the experimenter cannot feasibly determine if the perturbation they selected is the ideal
218 or optimal one (i.e. the one with the largest effect on RVPh) without performing a very large num-
219 ber of numerical experiments. By contrast, in an adjoint sensitivity experiment, the experimenter
220 selects a quantity of interest (e.g. annual mean RVPh) and uses an adjoint approach to calculate
221 *gradients* or *sensitivities*. The sensitivity fields indicate the perturbations with the largest possible

222 linear impact on RVPh. For examples of adjoint sensitivity experiments, see Verdy et al. (2014);
 223 Sévellec and Fedorov (2015); Jones et al. (2018), and many others. We refer the reader to these
 224 works for a more thorough and general description to adjoint modeling (Thacker and Long 1988;
 225 Marotzke et al. 1999b; Heimbach 2008; Mazloff et al. 2010; Griewank and Walther 2012; Verdy
 226 et al. 2014; Forget et al. 2015a; Fukumori et al. 2015; Jones et al. 2018, for example).

227 We perform a set of such adjoint sensitivity experiments in order to examine the sensitivity of
 228 RVPh to subsurface ocean properties. The objective function is defined as the annual- and volume-
 229 mean RVPh:

$$\tilde{J} = \frac{1}{V\Delta t} \int_V \int_{\Delta t} \rho_0 c_p \theta(\mathbf{r}, t) dt dV, \quad (1)$$

230 where ρ_0 is the reference density, c_p is the heat capacity of seawater, θ is the potential temperature,
 231 \mathbf{r} is the position vector, t is the time, V is the control volume, and Δt is the time period of the
 232 integration. For convenience, we scale \tilde{J} by the constant $\rho_0 c_p$, so RVPh = $J = \tilde{J} / \rho_0 c_p$, meaning
 233 that RVPh has units of $^{\circ}C$.

234 We compute an ensemble of six adjoint sensitivity experiments, with the objective function
 235 defined over the last year of each run, i.e. from 1 January to 31 December, with objective function
 236 years ranging from 2006 through 2011. Each experiment spans a minimum of 15 years, up to a
 237 maximum of 20 years. We allow the RVP to vary by ensemble member based on the results of
 238 the passive tracer experiments. Our ECCOV4 adjoint model calculates the sensitivities of these
 239 objective functions to a set of independent variables, including temperature ($\partial J / \partial T$) and salinity
 240 ($\partial J / \partial S$); the sensitivity fields vary with space (latitude, longitude, depth) and time. We use 14-day
 241 averaged sensitivity fields throughout.

242 3. Identifying the recently ventilated subsurface ocean

243 We use a six-member ensemble of passive tracer experiments with release years ranging from
244 1996 to 2001 to identify the RVP in ECCOv4. The ensemble mean, annual mean tracer distribution
245 after 10 years of integration (Figure 2) highlights the ventilation pathways from the Southern
246 Ocean mixed layer into the subsurface thermocline.

247 The normalized tracer distribution features several cores, i.e. local maxima with some degree
248 of spatial coherence across latitudes and longitudes (Supplemental Animation S1). In the Atlantic
249 sector, we find a core below the 1992-2011 maximum MLD in the subtropical latitudes (roughly
250 between 30°S-10°S) that drifts southwards before merging with a broad pattern that stretches
251 from the Weddell Sea, across the ACC, and into the subtropics (Figure 2(a)). The approximately
252 zonal Atlantic distribution bears the imprint of the convergence of the Brazil current and the ACC.
253 In the Indian sector, the tracer distribution is influenced by the Agulhas current and the broader
254 circulation of the South Indian Gyre that is characterized by relatively shallow overturning in
255 density space; here, we find the core of the distribution at roughly 500 m and densities lighter than
256 the $\sigma_0 = 26.9 \text{ kg m}^{-3}$ density surface (Figure 2(b)). In the Pacific sector, we find relatively large
257 values throughout the entire South Pacific Gyre (SPG), with two distinct cores. The core of the
258 distribution in the western SPG is found at densities lighter than $\sigma_0 = 26.9 \text{ kg m}^{-3}$ and is affected
259 by tracer that subducts in the Indian sector, whereas the core of the distribution in the eastern SPG
260 largely straddles the $\sigma_0 = 26.9 \text{ kg m}^{-3}$ line and is relatively less affected by tracer that subducts
261 in the Indian sector (Figure 2(c,d)). High tracer concentrations in the eastern region of the SPG
262 highlights the relatively efficient Eastern Pacific export pathway that was previously identified in
263 high-resolution simulations (Jones et al. 2016, Figure 8d).

264 In order to define the RVP, we use the annual mean tracer concentrations after 10 years of
265 transport and some additional physical and geographical criteria, selecting grid cells that satisfy
266 the following four conditions:

- 267 • be located below the maximum mixed layer over the entire ECCOv4-r2 period (i.e. 1992-
268 2011)
- 269 • tracer concentration is at least 10% of the global ocean maximum value
- 270 • be located in the Southeast Pacific, between 170°W-60°W and 60°S-20°S
- 271 • potential density is greater than or equal to $\sigma_0 = 26.9 \text{ kg m}^{-3}$

272 The $\sigma_0 = 26.9 \text{ kg m}^{-3}$ surface delineates lighter waters from waters that are at least as dense
273 as the SAMW. The resulting RVP for any given release year is a three-dimensional volume with
274 a lateral imprint that varies with depth (Figure 3 and 4). Between roughly 300-500m (Figure
275 3(a)-(c)), the areal extent of the RVP changes with depth and sits largely in the Southeast Pacific,
276 north of the regions with deep mixed layers. The structure of the RVP at these depths reflects the
277 subduction and ventilation pattern associated with the Eastern Pacific export pathway (Jones et al.
278 2016). Between roughly 500-700 m (Figure 3(d)-(e)), the RVP reaches its maximum areal extent,
279 covering a large fraction of the SPG.

280 1) THE RVP IS MORE GENERAL THAN SAMW

281 Although the RVP has considerable overlap with the density ranges associated with SAMW, it
282 is more general than SAMW alone. Our passive tracers ventilate a wide range of water masses,
283 including SAMW, AAIW, and the lightest part of the Circumpolar Deep Water (CDW). In this
284 way, our RVP approach is broader than an approach focused on a particular density range, in that
285 it allows us to consider a wider range of ventilated water mass types than SAMW alone. Because

286 RVP_h is the heat content of a fixed volume, RVP_h is a measure of the heat distribution in the
287 target region, as RVP_h may be affected by both isopycnal heave and by changes in properties
288 along isopycnals. RVP_h may have different sensitivities than the SAMW heat content, which may
289 be affected by changes in the volume of SAMW and/or changes in the properties of water in the
290 SAMW density range. We further explore this distinction in section 5.

291 Having defined the RVP in ECCOv4, we can now perform a set of adjoint sensitivity experiments
292 using the adjoint capability of the ECCOv4 model setup.

293 **4. Sensitivities of subsurface heat content to local and remote anomalies**

294 In this section, we examine the sensitivity of RVP_h to changes in temperature and salinity, de-
295 composed into changes at constant density (i.e. kinematic sensitivities) and changes with varying
296 density (i.e. dynamic sensitivities). In subsection a, we show how sensitivities to temperature and
297 salinity perturbations can be cast in terms of kinematic and dynamic sensitivities. In subsection b,
298 we investigate the spatial and temporal structure of the kinematic sensitivities, focusing on both the
299 subsurface and the surface. Finally, in subsection c, we examine the spatial and temporal structure
300 of the dynamic sensitivities, including regional patterns in the subsurface and at the surface. In
301 this analysis, we use the time-variable -0.25 m ECCOv4 sea surface height contour as a proxy for
302 the Subantarctic Front (SAF) that roughly divides the Southern Ocean into two regions - one dom-
303 inated by gyre-like circulation and another region dominated by the circumpolar flow associated
304 with the ACC (Kim and Orsi 2014).

305 *a. Defining kinematic and dynamic sensitivities*

306 Following Marotzke et al. (1999b) and Jones et al. (2018), we decompose the adjoint sensitivity
307 fields into sensitivities to changes that propagate along isopycnals (i.e. kinematic) and sensitivities

308 to changes in density (i.e. dynamic). Writing the objective function in terms of density and
 309 temperature $J = J[\rho(T, S), T]$ allows us to write the sensitivities as follows:

$$\left(\frac{\partial J}{\partial T}\right)_S = \left(\frac{\partial J}{\partial \rho}\right)_T \left(\frac{\partial \rho}{\partial T}\right)_S + \left(\frac{\partial J}{\partial T}\right)_\rho. \quad (2)$$

310 The first term on the right-hand side of equation 2 is the “dynamic” component of the sensitivity
 311 (i.e. sensitivity to changes in density), and the second term on the right-hand side is the “kine-
 312 matic” component (i.e. dynamically-inactive sensitivities to temperature anomalies). Using the
 313 coefficient of thermal expansion α and coefficient of haline contraction β , defined as

$$\alpha \equiv -\frac{1}{\rho} \left(\frac{\partial \rho}{\partial T}\right)_S \quad \text{and} \quad \beta \equiv \frac{1}{\rho} \left(\frac{\partial \rho}{\partial S}\right)_T, \quad (3)$$

314 we can write

$$\left(\frac{\partial J}{\partial S}\right)_T = \left(\frac{\partial J}{\partial \rho}\right)_T \left(\frac{\partial \rho}{\partial S}\right)_T = \beta \rho \left(\frac{\partial J}{\partial \rho}\right)_T, \quad (4)$$

315 and the dynamic sensitivity becomes:

$$F_{dyn} = \left(\frac{\partial J}{\partial \rho}\right)_T \left(\frac{\partial \rho}{\partial T}\right)_S = \frac{1}{\beta \rho} \left(\frac{\partial J}{\partial S}\right)_T \left(\frac{\partial \rho}{\partial T}\right)_S = -\frac{\alpha}{\beta} \left(\frac{\partial J}{\partial S}\right)_T. \quad (5)$$

316 We can write the kinematic sensitivity as:

$$F_{kin} = \left(\frac{\partial J}{\partial T}\right)_S + \frac{\alpha}{\beta} \left(\frac{\partial J}{\partial S}\right)_T. \quad (6)$$

317 Physically, kinematic sensitivities indicate the linear response of the objective function to the
 318 simultaneous application of a small temperature change and a compensating salinity change of
 319 the form $\Delta S = \Delta T \alpha / \beta$, such that density remains constant following the linearized equation of
 320 state for seawater, $\rho = \rho_0(1 - \alpha \Delta T + \beta \Delta S)$. We can refer to these perturbations as “density-
 321 compensated temperature anomalies”. In contrast, dynamic sensitivities indicate the linear re-
 322 sponse of the objective function to the application of a temperature change ΔT or a density-
 323 equivalent salinity change of $\Delta S = -\Delta T \alpha / \beta$ in the equation of state. The linear response is

324 given by $\Delta J = F_{dyn}\Delta T = F_{dyn}(-\Delta S\beta/\alpha)$. We use 14-day averaged, three-dimensional α/β fields
325 derived from ECCOv4-r2 potential temperatures and salinities using the TEOS-10 toolbox (Mc-
326 Dougall and Barker 2011). Next, we examine the kinematic and dynamic sensitivities of RVPh.

327 In this paper, we follow the naming and conceptual conventions established in the adjoint mod-
328 eling literature, specifically the use of kinematic and dynamic sensitivities (Marotzke et al. 1999a;
329 Jones et al. 2018, e.g.). Kinematic sensitivities are conceptually similar to sensitivities to “spice”
330 anomalies (Flament 2002), and dynamic sensitivities are conceptually similar to sensitivities to
331 “heave” anomalies (Bindoff and Mcdougall 1994). However, despite their resemblance, it would
332 be misleading to conflate kinematic sensitivities with sensitivities to spice anomalies, and it would
333 be misleading to conflate dynamic sensitivities with sensitivities to heave anomalies. Their deriva-
334 tions and resulting definitions are not rigorously identical. In addition, there is a difference in how
335 these quantities are normally used; spice and heave are typically used to decompose local potential
336 temperature anomalies into these two components, whereas kinematic and dynamic adjoint sensi-
337 tivities are more generally used to show impacts on an objective function over different spatial and
338 temporal lags.

339 At present, adjoint sensitivity fields in ECCOv4 do *not* include sensitivity to changes in mixing
340 as parameterized by the GGL mixed layer turbulence closure scheme. Also, the sensitivity fields
341 do *not* include the sensitivity to changes in sea ice. The adjoint sensitivity calculations essentially
342 treat GGL mixing and sea ice as fixed processes. We apply a mask of the form $(1 - f)$, where f is
343 the local sea ice concentration, to all surface sensitivity fields to account for the lack of sensitivity
344 to sea ice change.

345 *b. Sensitivity to changes at constant density*

346 Kinematic sensitivity fields approximately indicate potential source water pathways. More
347 specifically, one can think of the kinematic sensitivity fields as indicating the eventual response of
348 annual mean RVP heat content to a spatially uniform, density-compensated potential temperature
349 perturbation that is sustained for some time (in our case, two weeks) and allowed to propagate.
350 Regions with zero sensitivity cannot affect RVP; such regions are not connected to the RVP via
351 advection and mixing on the associated timescales. The kinematic sensitivity fields are positive or
352 zero nearly everywhere; an increase/decrease in temperature in regions with non-zero sensitivities
353 eventually increases/decreases RVP heat content on the indicated lag timescale (Figure 5).

354 The near-surface kinematic sensitivity fields highlight the potential propagation pathways of
355 anomalies into the SAMW formation regions, where they can be subducted below the mixed layer
356 and exported into the thermocline (Figure 5, left column, and Supplemental Animation S2). In the
357 Pacific basin, the largest near-surface sensitivity fields tend to be found just north of the SAF proxy,
358 within or upstream of regions of deep mixed layers and mostly south of the RVP areal extent. In
359 the Indian basin, the largest near-surface sensitivity fields are found along the SAF proxy or just
360 south of it. The fields cross over the SAF around Campbell Plateau and South Australian Basin,
361 suggesting cross-front exchange in this region.

362 Density-compensated anomalies cannot typically propagate from directly above the RVP into
363 the RVP itself on the timescales considered here; they are not typically advected into the regions
364 of deep mixing. On timescales longer than 10 years, the near-surface sensitivities extend across the
365 entire Southern Ocean, putting a lower bound on the temperature anomaly propagation timescale
366 from the Atlantic to the RVP (Figure 5, left column). On timescales longer than roughly 5-6
367 years, we find sensitivities south of the SAF proxy in the Indian basin; here, wind stress may

368 advect anomalies across the SAF via Ekman transport. On shorter timescales, the sensitivity fields
369 are more localized around the southeast Pacific mixed layer region and are typically smaller in
370 magnitude relative to the deeper levels. Temperature anomalies can only affect RVPh if they
371 have sufficient time to propagate into the mixed layer, subduct, and get exported; only very local,
372 targeted anomalies can affect RVPh on timescales shorter than 1-2 years. The persistent local
373 maximum in the southeast Pacific indicates a relatively rapid route from the surface into the RVP,
374 which is consistent with a well-documented subduction and export pathway in that location (Sallée
375 et al. 2010b).

376 The subsurface sensitivity fields highlight the long residence time of local hypothetical pertur-
377 bations in the subsurface of the gyre, as well as the pathways of subsurface ocean advection into
378 the RVP (Figure 5, right column, and Supplemental Animation S3). On timescales longer than 10
379 years, we find sensitivities extending along the East Australian Current and, in contrast with the
380 surface sensitivities, sensitivities along the Agulhas Current and associated retroflexion as well.
381 Surface anomalies in the Agulhas Current cannot affect RVPh on the timescales considered here,
382 but anomalies in the subsurface (here, roughly 550 m) can eventually alter RVPh. We also find
383 some sensitivity at this depth extending along the Brazil current. Notably, the Agulhas current is
384 the only major Southern Hemispheric western boundary current with zero kinematic sensitivity in
385 the near-surface.

386 The global mean RMS kinematic sensitivity decreases with timescale (Figure 6(a)). It is reason-
387 ably well described ($R^2 > 0.99$) by an exponential function with a decay rate of about 10 years.
388 The decay partly reflects the fact that as we consider longer timescales, RVPh becomes sensitive
389 to a larger fraction of the ocean, so the global RMS sensitivity decreases. The decay also partly
390 reflects the tendency of air-sea exchange, represented in ECCOv4 as bulk formulae with a pre-
391 scribed set of atmospheric variables, to dampen potential temperature anomalies at the surface

392 and thereby reducing the sensitivities. The linear change in sensitivity between lag 0 and lag 1 yr
393 reflects the one-year integration period over which the objective function is calculated. There is
394 no sensitivity to anomalies after year 1, after the integration has finished. The ensemble standard
395 deviation is small, indicating a relatively low level of interannual variability in sensitivity across
396 our six-member ensemble.

397 We find non-zero sensitivities to hypothetical anomalies within the local RVP throughout the
398 entire 16-year adjoint sensitivity experiment, indicating that RVPh is sensitive to local density-
399 compensated temperature anomalies on timescales of at least 16 years (Figure 6(b)). The ensemble
400 mean RMS local sensitivity time series is well-described ($R^2 > 0.99$) by a two-term exponential
401 with decay rates of 4.4 years and 10.9 years. The non-local RMS sensitivities outside of the
402 RVP exceed the local sensitivities on timescales longer than roughly 5 years (Figure 6(b)). RMS
403 sensitivities outside of the MLD mask are larger than those within the MLD mask on timescales
404 shorter than about 8 years (Figure 6(c)). This is largely due to the fact that sensitivities exist below
405 the surface, e.g. in the RVP itself, where the overlying mixed layers are typically shallow.

406 Outside of the RVP, we mostly find non-zero sensitivities just north of the SAF proxy in all three
407 ocean basins, in what may be considered the northern extent of the ACC (Figure 6(d)). The near-
408 surface sensitivity fields display a clear seasonal cycle, with the RMS mean peaking in August
409 in the Pacific and Indian basins, during the strong mixing phase that occurs as the mixed layer
410 deepens before reaching its maximum depth in mid-September (Figure 6e). The sensitivity fields
411 spread westward with lead time, reflecting the advective timescale between basins (Figure 6(e,f)).
412 The RMS sensitivity in the West Pacific exceeds the East Pacific value on timescales longer than
413 roughly 4.4 years.

414 *c. Sensitivity to changes in density*

415 The dynamic sensitivity fields indicate patterns of density change that can alter RVPh, poten-
416 tially by inducing changes in isopycnal tilt and thereby altering the associated transport and heat
417 convergence into the RVP. More specifically, one can think of the dynamic sensitivity fields as
418 indicating the eventual response of annual mean RVP heat content to a spatially uniform potential
419 temperature perturbation, or a density-equivalent salinity perturbation, that is sustained for some
420 time (two weeks, as with the kinematic sensitivity case) and allowed to affect the oceanic density
421 structure. Regions of zero sensitivity cannot affect RVPh; such regions are not dynamically con-
422 nected to the RVP. The dynamic sensitivity fields are both positive and negative, with the dipoles
423 highlighting regions where a change in isopycnal tilt will change the associated circulation and
424 ultimately RVPh (Figure 7).

425 The near-surface dynamic sensitivity fields are mostly negative across all lags, with local ex-
426 ceptions south of Australia and in the eastern tropical Pacific (Figure 7, left column). Negative
427 values indicate regions where a hypothetical temperature increase, which will decrease density,
428 will ultimately decrease RVP heat content. Similarly, in these regions a hypothetical temperature
429 decrease, which will increase density, will ultimately increase RVP heat content. It is important
430 to note that, due to technical limitations, our adjoint sensitivity fields *do not* represent non-linear
431 changes. They *do* reflect changes in circulation and diffusion. So the negative near-surface values
432 may represent the fact that, even under fixed mixing conditions, relatively lighter water may not
433 reach the depths of the RVP as readily as relatively denser water, where “relative” refers to the
434 background ECCOv4 state around which the adjoint sensitivities are calculated. Alternatively, the
435 negative near-surface values may represent a hypothetical decrease in RVP heat convergence in-
436 duced by a surface decrease in density, or the values may represent a hypothetical increase in RVP

437 heat convergence induced by a surface increase in density. As with the kinematic sensitivity fields,
438 on shorter timescales the dynamic sensitivities become increasingly localized to the southeastern
439 edge of the RVP, near the southern tip of South America.

440 In contrast with the near-surface kinematic sensitivity fields, the near-surface dynamic sensitiv-
441 ity fields feature a persistent negative local minimum along the western coast of South America
442 (Figure 7, left column, and Supplemental Animation S4). Considered together with the small
443 positive values in the eastern tropical Pacific, this dipole reflects a sensitivity to the across-shelf
444 pressure gradient. Variations in the across-shelf pressure gradients are associated with changes
445 in basin-scale pressure gradients and the associated basin-scale circulation, which can ultimately
446 change heat convergence and thus heat content within a selected ocean volume (Fukumori et al.
447 2015; Jones et al. 2018; Hughes et al. 2018).

448 The subsurface dynamic sensitivity fields highlight the sensitivity of annual mean RVP heat con-
449 tent to basin-wide density contrasts, equivalently expressed as tilted basin-scale isopycnal surfaces
450 (Figure 7, right column, and Supplemental Animation S5). This basin-scale structure is associated
451 with the circulation of the SPG, which is in part maintained by pressure gradients induced by wind
452 stress curl. We find a persistent sensitivity dipole stretched across the RVP, with positive values
453 to the east and negative values to the west. The positive values reach into the tropics and extend
454 westward with timescale, across both the Pacific and Indian basins. To illustrate the structure of
455 these fields, consider a hypothetical potential temperature anomaly characterized by warming to
456 the east of the RVP and cooling to the west of the RVP, imposed on the model vertical level cen-
457 tered at 553 m (Figure 7(d)). The warming to the east would decrease density at 553 m and, based
458 on the positive sign of the sensitivity field, ultimately contribute to an increase RVPh. The cooling
459 to the west would increase density at 553 m and, based on the negative sign of the sensitivity field,
460 it would also increase RVPh. The change in RVPh induced by any anomaly is the product of the

461 sensitivity field and the imposed anomaly, i.e. $\Delta J = F_{dyn}\Delta T$. In this scenario, we have imposed
462 isopycnal deepening to the east and isopycnal shoaling to the west. In the RVP, isopycnal surfaces
463 at roughly 500-600 m tend to shoal from west to east, so our imposed perturbation alters isopycnal
464 surfaces locally, ultimately changing transport and increasing heat convergence in the RVP (Jones
465 et al. 2018).

466 The subsurface sensitivity fields also feature a persistent sensitivity along the western coast of
467 South America (Figure 7, right column). In contrast to the near-surface fields, which are fairly
468 consistently negative along the shelf, the along-shelf subsurface fields are positive to the north and
469 negative to the south. The north-south sign contrast indicates a sensitivity to barotropic structure,
470 whereas the surface-subsurface sign contrast highlights an overall sensitivity to baroclinic den-
471 sity structure above the continental shelf. In addition, the subsurface fields display characteristic
472 fingerprints of baroclinic Rossby waves, as seen by westward propagating positive anomalies at
473 depth (Supplemental Animation S5). As with the surface fields, on shorter timescales the subsur-
474 face dynamic sensitivities become increasingly localized, albeit with a different structure than the
475 surface fields. The subsurface fields are localized around the edge of the RVP, indicating a sensi-
476 tivity to density contrasts across the RVP that can alter fluxes across the boundary of the RVP, and
477 the subsurface sensitivities are also localized along the western coast of South America, indicating
478 a short-timescale sensitivity to density changes along the continental shelf.

479 The globally averaged RMS dynamic sensitivity increases with timescale, reaching a maximum
480 at roughly 8.7 years (Figure 8(a)). Much of this sensitivity comes from outside the RVP, partic-
481 ularly near its boundary (Figure 8(b)). RMS sensitivity is similar inside and outside of the MLD
482 mask, indicating that when considering RVP, we need to study dynamic changes both inside and
483 far outside of the regions of deep mixing (Figure 8(c)). The RMS sensitivity is persistently larger
484 north of the SAF proxy, although much of this is located just north of the SAF, and the RMS

485 sensitivity south of the SAF increases roughly linearly with timescale (Figure 8(d)). The near-
486 surface fields also display a seasonal cycle, with similar timings as the kinematic fields (Figure
487 8(e)). Notably, the RMS dynamic sensitivity is persistently higher in the West Pacific than in the
488 East Pacific, indicating the importance of dynamic basin-scale changes (Figure 8(h)). The RMS
489 sensitivity in the Indian and Atlantic basins increases with timescale, although the values are neg-
490 ligibly small (less than 3% of the maximum) for short timescales (about 2.5 years for the Indian
491 basin and 5 years for the Atlantic basin).

492 **5. Discussion**

493 In the canonical view of Southern Ocean meridional overturning circulation (MOC), Circum-
494 polar Deep Water upwells south of the ACC, where it is brought to the surface and exported
495 northwards; this water is modified by air-sea fluxes and is ultimately subducted as SAMW and
496 AAIW (Marshall and Speer 2012). As a result of this overturning circulation, the properties of
497 SAMW and AAIW are potentially sensitive to anomalies in near-Antarctic waters. For example,
498 the variability of the Amundsen Sea low (ASL) can affect the interannual and interdecadal vari-
499 ability of SAMW in the Southeast Pacific via cross-frontal Ekman transport of Antarctic surface
500 waters (Garabato et al. 2009; Close et al. 2013). In 2008-2010, a deep ASL enhanced the merid-
501 ional wind-driven sea ice export from the eastern Ross Sea; the sea ice melt introduced a cold
502 surface freshwater anomaly that was advected across the PF and SAF by Ekman transport and
503 then transported into the SAMW formation region by the ACC (Cerovecki et al. 2019). In this
504 context, our adjoint sensitivity results may appear surprising, in that they show relatively weak
505 sensitivities to anomalies in the Ross Sea. Our results are not inconsistent with those studies, but
506 there are several factors to consider when comparing our results with those obtained using other
507 approaches, as discussed below.

508 *a. RVP is a fixed-volume quantity*

509 Our control volume is fixed relative to the model grid. Although RVP captures the mean position
510 of the ventilated water, it does not move with isopycnal heave. Because it overlaps with both
511 SAMW and AAIW, it is more general than either water mass, but we must be careful not to
512 conflate SAMW/AAIW with the RVP. Isopycnal heave in the subtropical gyre can affect RVP
513 without necessarily changing the heat content of the recently subducted SAMW. However, RVP
514 can still tell us something about subduction. The majority of recent heat uptake by SAMW is
515 driven by a thickening of the associated isopycnal layers, driven by changes in wind forcing and
516 subduction in the deep mixed layer region Gao et al. (2018). Considering SAMW in the Pacific
517 basin, its local mean temperature is correlated with remote forcing (e.g. air-sea heat flux, wind
518 stress) with a lag that is attributed to transport, whereas its total heat content is controlled largely
519 by layer thickness, which is driven by local wintertime forcing (Meijers et al. 2019). These results
520 are consistent with the our adjoint sensitivity fields, which largely capture mechanisms that can
521 affect mean temperature within the SAMW as opposed to those that can affect total heat content
522 via changing layer thickness. It would be useful to examine the sensitivities in an adjoint model
523 that uses isopycnal surfaces as its vertical coordinate, but this is beyond the scope of this paper.

524 *b. Zonal flow dominates meridional overturning*

525 The largely zonal volume transport of the ACC is at least an order of magnitude larger than the
526 volume transport associated with the MOC (Talley 2013; Donohue et al. 2016). As such, we might
527 expect our adjoint sensitivity fields to reflect the dominance of ACC transport in the Southeast
528 Pacific. According to these fields, sensitivity to high-latitude processes is small but nonzero. To
529 examine the impacts of actual temperature and salinity anomalies on RVP, one could examine
530 the combination of sensitivity fields together with temperature and/or salinity anomaly fields. In

531 this work, we focus on the sensitivity fields themselves, as these could potentially be combined
532 with a large variety of anomaly fields in order to address different questions (e.g. how does the
533 SAM forcing pattern affect RVPh across different timescales?)

534 *c. Cross-front exchange rates differ between data products*

535 Cross-front exchange in the SO is highly localized, occurring in relatively narrow longitude
536 bands in the lee of bathymetric features (Thompson and Sallée 2012). The propagation of anoma-
537 lies from the Ross Gyre to the subtropics occurs largely via two distinct exchange windows in the
538 Southeast Pacific and the central Pacific; on timescales of roughly 1-3 years, the central Pacific
539 pathway enables transport from Antarctic surface waters to the deep mixed layer region (Cerovecki
540 et al. 2019). The subsurface exchange pathway in the central Pacific (around the Eltanin fracture
541 zone, between roughly 110-160°W) is driven by enhanced diapycnal mixing near the relatively
542 rough topography and temporal circulation variability on timescales longer than 90 days (McAu-
543 field 2019). Because of its relatively coarse resolution, it is possible that ECCOv4-r2 may have
544 a lower cross-frontal exchange rate than that of higher-resolution data products, but a lack of ob-
545 servational data constraints makes it challenging to discriminate amongst estimates. A thorough,
546 quantitative comparison of exchange rates between ECCOv4-r2 and other data products would be
547 a useful addition to this work.

548 *d. Mixed layer depth*

549 In this work, we calculate mixed layer depth using a criteria based on the density change associ-
550 ated with a temperature variation of $\Delta T = 0.8^\circ\text{C}$ (Kara et al. 2000). Compared with other methods,
551 this threshold approach tends to be biased towards deeper values (Forget et al. 2015c, supporting
552 information). Because we discard all tracer above the maximum mixed layer, this implies that our

553 estimate of the subducted volume may be somewhat conservative. It is possible that our results
554 would be different using another mixed layer scheme. That being said, the stratification and mixed
555 layer properties in ECCOv4 compare well spatially with in-situ profiles (Forget et al. 2015c, Fig.
556 6).

557 *e. Adjoint sensitivities use fixed vertical mixing and sea ice*

558 At present, adjoint sensitivity fields in ECCOv4 do *not* include sensitivities to changes in mix-
559 ing as parameterized by the GGL mixed layer turbulence closure scheme. Also, the sensitivity
560 fields do *not* include the sensitivity to changes in sea ice. Although the forward and adjoint runs
561 do feature dynamic sea ice and vertical mixing as parameterized by GLL, the adjoint sensitivity
562 calculations essentially treat them as fixed processes. Any processes that affect RVPh primar-
563 ily through *changing* sea ice concentration and/or vertical mixing will not be represented in our
564 sensitivity fields.

565 **6. Summary and conclusions**

566 We used numerical passive tracer experiments and physical state variables (i.e. mixed layer
567 depth, potential density, potential vorticity) in an observationally-constrained state estimate to
568 identify the recently ventilated Eastern Pacific sector of the Southern Ocean (RVP), which is a
569 relatively efficient export pathway from the surface ocean into the subsurface thermocline. The
570 RVP, defined on a 10-year timescale, is located north of the -0.25 m sea surface height contour
571 (i.e. the SAF proxy) and north of the deep mixed layer regions, highlighting the ventilation path-
572 way from the tip of South America, along the eastern Pacific boundary and out across the South
573 Pacific Gyre (SPG) in the subsurface. The RVP varies with depth, reaching maximum areal extent
574 between 500-600 m, and it features some variation with tracer release year, mostly in its western

575 extent. The overall spatial pattern of the subducted tracer is consistent with estimates from an
576 eddy-permitting model (Jones et al. 2016).

577 We used the adjoint capabilities of MITgcm to calculate the sensitivities of annual mean heat
578 content within the fixed volume RVP (i.e. RVPh) to anomalies in potential temperature and salin-
579 ity. These sensitivities are four-dimensional (i.e. latitude, longitude, depth, and time) and indicate
580 the anomaly patterns that can have the largest potential impact on RVPh after the appropriate lag
581 time has elapsed (Figure 9). In terms of sensitivities to surface anomalies, RVPh is most sensitive
582 to anomalies along the SAF proxy, upstream of the subduction hotspot in the Southeast Pacific.
583 The sensitivity signal crosses the SAF proxy around Campbell Plateau and just south of Australia,
584 indicating possible wind-driven cross-frontal exchange in that region. This result is consistent
585 with estimates of the spatial pattern of meridional Ekman transport of atmospheric carbon in an
586 eddy-permitting state estimate (Ito et al. 2010). In terms of sensitivities to subsurface anomalies,
587 RVPh is most sensitive to basin-scale changes in density, as indicated by the persistent dipole in
588 subsurface dynamic sensitivity (Figure 7). The sensitivity dipole is centered around the same lati-
589 tudes as the RVP, extending upstream along the ACC and northwards into the tropical Pacific with
590 increasing timescale. This persistent dipole implies that property gradients between the SPG and
591 the ACC are important for interannual variability in RVPh.

592 By the end of the 21st century, Southern Ocean wind stress is expected to strengthen in magni-
593 tude and move poleward, resulting in a poleward shift of the gyres, and mixed layers are expected
594 to shoal (Meijers 2013). Our results suggest that the resulting subtropical, basin-scale temperature
595 and salinity changes induced by the expected shifts in wind stress and heat flux can have a consid-
596 erable impact on the heat distribution of the ventilated Southeast Pacific, across the density ranges
597 of the base of the SAMW, AAIW, and the lightest CDW. In a companion manuscript, we examine
598 the sensitivities of RVP heat content to changes in surface forcing (Jones et al. 2019).

599 *Acknowledgments.* This study is supported by grants from the Natural Environment Research
600 Council (NERC), including [1] The North Atlantic Climate System Integrated Study (ACSIS)
601 (grant NE/N018028/1, authors DJ, ES), [2] Securing Multidisciplinary Understanding and Pre-
602 diction of Hiatus and Surge events (SMURPHS) (grant NE/N006038/1, author EB), and [3] Ocean
603 Regulation of Climate by Heat and Carbon Sequestration and Transports (ORCHESTRA) (grant
604 NE/N018095/1, authors EB, AM, SJ). GF is supported by NASA award #6937342 and Simons
605 Foundation award #549931. Numerical model runs were carried out on ARCHER, the UK national
606 HPC facility [<http://archer.ac.uk/>]. Adjoint code was generated using the TAF software tool,
607 created and maintained by FastOpt GmbH [<http://www.fastopt.com/>]. We used the gcmfaces
608 package for plotting and analysis (<https://github.com/gaelforget/gcmfaces>). The authors
609 wish to thank two anonymous reviewers whose comments greatly improved the quality of this
610 paper.

611 **Data availability statement:** The model used here is an instance of the ECCOv4-r2 state es-
612 timate (<https://github.com/gaelforget/ECCOv4>) as an instance of the MIT general circula-
613 tion model (MITgcm, <http://mitgcm.org/>). Specific model configuration files, input data, and
614 sample output available via Zenodo (Jones 2020).

615 **References**

616 Armour, K. C., J. Marshall, J. R. Scott, A. Donohoe, and E. R. Newsom, 2016: Southern Ocean
617 warming delayed by circumpolar upwelling and equatorward transport. *Nature Geoscience*,
618 **9** (7), 549–554, doi:10.1038/ngeo2731, URL <http://www.nature.com/articles/ngeo2731>.

619 Bindoff, N. L., and T. J. Mcdougall, 1994: Diagnosing Climate Change and Ocean Ven-
620 tilation Using Hydrographic Data. *Journal of Physical Oceanography*, **24** (6), 1137–

621 1152, doi:10.1175/1520-0485(1994)024<1137:DCCAOV>2.0.CO;2, URL [https://doi.org/10.1175/1520-0485\(1994\)024<1137:DCCAOV>2.0.CO;2](https://doi.org/10.1175/1520-0485(1994)024<1137:DCCAOV>2.0.CO;2).

622

623 Cerovečki, I., and M. Mazloff, 2015: The spatiotemporal structure of diabatic processes governing
624 the evolution of Subantarctic Mode Water in the Southern Ocean. *Journal of Physical Oceanog-*
625 *raphy*, **46**, 683–710, doi:10.1175/JPO-D-14-0243.1.

626 Cerovecki, I., A. J. S. Meijers, M. R. Mazloff, S. T. Gille, V. M. Tamsitt, P. R. Holland, and V. M.
627 Tamsitt, 2019: The effects of enhanced sea ice export from the Ross Sea on recent cooling
628 and freshening of the Southeast Pacific. *Journal of Climate*, JCLI-D-18-0205.1, doi:10.1175/
629 JCLI-D-18-0205.1.

630 Cerovecki, I., L. D. Talley, M. R. Mazloff, and G. Maze, 2013: Subantarctic Mode Water Forma-
631 tion, Destruction, and Export in the Eddy-Permitting Southern Ocean State Estimate. *Journal*
632 *of Physical Oceanography*, **43** (7), 1485–1511, doi:10.1175/jpo-d-12-0121.1.

633 Cessi, P., and P. Otheguy, 2003: Oceanic teleconnections: Remote response to decadal wind forc-
634 ing. *Journal of Physical Oceanography*, **33** (8), 1604–1617.

635 Close, S. E., A. C. Naveira Garabato, E. L. McDonagh, B. A. King, M. Biuw, and L. Boehme,
636 2013: Control of Mode and Intermediate Water Mass Properties in Drake Passage by the
637 Amundsen Sea Low. *Journal of Climate*, **26** (14), 5102–5123, doi:10.1175/JCLI-D-12-00346.1,
638 URL <http://journals.ametsoc.org/doi/10.1175/JCLI-D-12-00346.1>.

639 Dee, D. P., and Coauthors, 2011: The ERA-Interim reanalysis: configuration and performance of
640 the data assimilation system. *Quarterly Journal of the Royal Meteorological Society*, **137** (656),
641 553–597, doi:10.1002/qj.828.

642 Donohue, K. A., K. L. Tracey, D. R. Watts, M. P. Chidichimo, and T. K. Chereskin, 2016: Mean
643 Antarctic Circumpolar Current transport measured in Drake Passage: MEAN ACC TRANS-
644 PORT. *Geophysical Research Letters*, **43** (22), 11,760–11,767, doi:10.1002/2016GL070319,
645 URL <http://doi.wiley.com/10.1002/2016GL070319>.

646 Downes, S. M., N. L. Bindoff, S. M. Downes, N. L. Bindoff, and S. R. Rintoul, 2009: Impacts
647 of Climate Change on the Subduction of Mode and Intermediate Water Masses in the Southern
648 Ocean. *dx.doi.org*, **22** (12), 3289–3302 PB –, doi:10.1175/2008JCLI2653.1.

649 Durack, P. J., and S. E. Wijffels, 2010: Fifty-Year Trends in Global Ocean Salinities and Their
650 Relationship to Broad-Scale Warming. *Journal of Climate*, **23** (16), 4342–4362, doi:10.1175/
651 2010JCLI3377.1, URL <https://journals.ametsoc.org/doi/full/10.1175/2010jcli3377.1>.

652 Errico, R. M., 1997: What Is an Adjoint Model? *Bulletin of the American Meteorological Society*,
653 **78** (11), 2577–2591, doi:10.1175/1520-0477(1997)078<2577:wiaam>2.0.co;2.

654 Fekete, B. M., C. J. Vörösmarty, and W. Grabs, 2002: High-resolution fields of global runoff com-
655 bining observed river discharge and simulated water balances. *Global Biogeochemical Cycles*,
656 **16** (3), 15–1–15–10, doi:10.1029/1999GB001254.

657 Flament, P., 2002: A state variable for characterizing water masses and their diffu-
658 sive stability: spiciness. *Progress in Oceanography*, **54** (1), 493 – 501, doi:[https://doi.org/10.1016/S0079-6611\(02\)00065-4](https://doi.org/10.1016/S0079-6611(02)00065-4), URL <http://www.sciencedirect.com/science/article/pii/S0079661102000654>.

659
660

661 Forget, G., J. M. Campin, P. Heimbach, C. N. Hill, R. M. Ponte, and C. Wunsch, 2015a: ECCO
662 version 4: an integrated framework for non-linear inverse modeling and global ocean state esti-
663 mation. *Geoscientific Model Development*, **8** (10), 3071–3104, doi:10.5194/gmd-8-3071-2015.

664 Forget, G., D. Ferreira, and X. Liang, 2015b: On the observability of turbulent transport rates by
665 Argo: supporting evidence from an inversion experiment. *Ocean Science Discussions*, **12** (3),
666 1107–1143, doi:10.5194/osd-12-1107-2015.

667 Forget, G., D. Ferreira, and X. Liang, 2015c: On the observability of turbulent transport rates
668 by Argo: supporting evidence from an inversion experiment. *Ocean Science*, **11** (5), 839–853,
669 doi:10.5194/os-11-839-2015.

670 Frölicher, T. L., J. L. Sarmiento, D. J. Paynter, J. P. Dunne, J. P. Krasting, and M. Winton, 2015:
671 Dominance of the Southern Ocean in Anthropogenic Carbon and Heat Uptake in CMIP5 Mod-
672 els. *Journal of Climate*, **28** (2), 862–886, doi:10.1175/jcli-d-14-00117.1.

673 Fukumori, I., O. Wang, W. Llovel, I. Fenty, and G. Forget, 2015: A near-uniform fluctuation of
674 ocean bottom pressure and sea level across the deep ocean basins of the Arctic Ocean and the
675 Nordic Seas. *Progress in Oceanography*, **134** (C), 152–172, doi:10.1016/j.pocean.2015.01.013.

676 Gao, L., S. R. Rintoul, and W. Yu, 2018: Recent wind-driven change in Subantarctic Mode
677 Water and its impact on ocean heat storage. *Nature Publishing Group*, 1–7, doi:10.1038/
678 s41558-017-0022-8.

679 Garabato, A. C. N., L. Jullion, D. P. Stevens, K. J. Heywood, and B. A. King, 2009: *Journal of*
680 *Climate*, **22** (13), 3661–3688, doi:10.1175/2009jcli2621.1.

681 Gaspar, P., Y. Grégoris, and J. M. Lefevre, 1990: A simple eddy kinetic energy model for
682 simulations of the oceanic vertical mixing: Tests at station Papa and long-term upper ocean
683 study site. *Journal of Geophysical Research: Atmospheres*, **95** (C9), 16 179–16 193, doi:
684 10.1029/JC095iC09p16179.

- 685 Gent, P. R., and J. C. McWilliams, 1990: Isopycnal Mixing in Ocean Circulation Models. *Journal*
686 *of Physical Oceanography*, **20** (1), 150–155, doi:10.1175/1520-0485(1990)020<0150:imiocm>
687 2.0.co;2.
- 688 Griewank, A., and A. Walther, 2012: *Evaluating Derivatives*. 2nd ed., Principles and Techniques
689 of Algorithmic Differentiation, Second Edition, Society for Industrial and Applied Mathemat-
690 ics, doi:10.1137/1.9780898717761.
- 691 Hanawa, K., and L. Talley, 2001: Mode Waters. *Ocean Circulation and Climate*, G. Siedler, and
692 J. Church, Eds., International Geophysics Series, 373–386.
- 693 Heimbach, P., 2008: *The MITgcm/ECCO adjoint modelling infrastructure*. Clivar Exchanges.
- 694 Helm, K. P., N. L. Bindoff, and J. A. Church, 2010: Changes in the global hydrological-cycle in-
695 ferred from ocean salinity. *Geophysical Research Letters*, **37** (18), doi:10.1029/2010GL044222,
696 URL <https://agupubs.onlinelibrary.wiley.com/doi/abs/10.1029/2010GL044222>.
- 697 Herraiz-Borreguero, L., and S. R. Rintoul, 2011: Subantarctic mode water: distribution and circu-
698 lation. *Ocean Dynamics*, **61** (1), 103–126, doi:10.1007/s10236-010-0352-9.
- 699 Hughes, C. W., J. Williams, A. Blaker, A. Coward, and V. Stepanov, 2018: A window on the deep
700 ocean: The special value of ocean bottom pressure for monitoring the large-scale, deep-ocean
701 circulation. *Progress in Oceanography*, **161**, 19–46, doi:10.1016/j.pocean.2018.01.011.
- 702 Ito, T., M. Woloszyn, and M. Mazloff, 2010: Anthropogenic carbon dioxide transport in the South-
703 ern Ocean driven by Ekman flow. *Nature*, **463**, 80, doi:10.1038/nature08687.
- 704 Iudicone, D., K. Rodgers, R. Schopp, and G. Madec, 2007: An exchange window for the injection
705 of Antarctic Intermediate Water into the South Pacific. *Journal of Physical Oceanography*, **37**,
706 31–49, doi:<http://dx.doi.org/10.1175/JPO2985.1>.

707 Johnson, G. C., and A. H. Orsi, 1997: Southwest Pacific Ocean Water-Mass Changes between
708 1968/69 and 1990/91*,. *JOURNAL OF CLIMATE*, **10**, 11.

709 Jones, D., 2020: DanJonesOcean/ecco_v4_r2_config: Initial release. Zenodo, URL [https://doi.org/](https://doi.org/10.5281/zenodo.3602900)
710 [10.5281/zenodo.3602900](https://doi.org/10.5281/zenodo.3602900), doi:10.5281/zenodo.3602900.

711 Jones, D. C., E. Boland, A. J. Meijers, G. Forget, S. A. Josey, J.-B. Sallee, and E. Shuckburgh,
712 2019: Heat distribution in the Southeast Pacific is only weakly sensitive to high-latitude heat flux
713 and wind stress. *Journal of Geophysical Research: Oceans*, **124**, doi:10.1029/2019JC015460,
714 URL <https://agupubs.onlinelibrary.wiley.com/doi/abs/10.1029/2019JC015460>.

715 Jones, D. C., G. Forget, B. Sinha, S. A. Josey, E. J. D. Boland, A. J. S. Meijers, and E. Shuckburgh,
716 2018: Local and Remote Influences on the Heat Content of the Labrador Sea: An Adjoint
717 Sensitivity Study. *Journal of Geophysical Research - Oceans*, **105 (2-3)**, 182, doi:10.1002/
718 [2018JC013774](https://doi.org/10.1002/2018JC013774).

719 Jones, D. C., A. J. S. Meijers, E. Shuckburgh, J.-B. Sallée, P. Haynes, E. K. McAufield, and
720 M. R. Mazloff, 2016: How does Subantarctic Mode Water ventilate the Southern Hemi-
721 sphere subtropics? *Journal of Geophysical Research - Oceans*, **121 (9)**, 6558–6582, doi:
722 [10.1002/2016jc011680](https://doi.org/10.1002/2016jc011680).

723 Kara, A. B., P. A. Rochford, and H. E. Hurlburt, 2000: An optimal definition for ocean mixed
724 layer depth. *Journal of Geophysical Research - Oceans*, **105 (C7)**, 16 803–16 821, doi:10.1029/
725 [2000JC900072](https://doi.org/10.1029/2000JC900072).

726 Karsten, R., and J. Marshall, 2002: Testing theories of the vertical stratification of the ACC against
727 observations. *Dynamics of Atmospheres and Oceans*, **36**, 233–246.

- 728 Katsumata, K., and M. Fukasawa, 2011: Changes in meridional fluxes and water proper-
729 ties in the Southern Hemisphere subtropical oceans between 1992/1995 and 2003/2004.
730 *Progress in Oceanography*, **89** (1), 61–91, doi:10.1016/j.pocean.2010.12.008, URL <http://www.sciencedirect.com/science/article/pii/S0079661110001606>.
731
- 732 Khatiwala, S., F. Primeau, and T. Hall, 2009: Reconstruction of the history of anthropogenic CO₂
733 concentrations in the ocean. *Nature*, **462** (7271), 346–349, doi:10.1038/nature08526.
- 734 Kim, Y. S., and A. H. Orsi, 2014: On the Variability of Antarctic Circumpolar Current Fronts
735 Inferred from 1992–2011 Altimetry*. *Journal of Physical Oceanography*, **44** (12), 3054–3071,
736 doi:10.1175/JPO-D-13-0217.1.
- 737 Large, W., and S. Yeager, 2009: The global climatology of an interannually varying air–sea flux
738 data set. *Climate Dynamics*, **33**, 341–364, doi:10.1007/s00382-008-0441-3.
- 739 Lenton, A., and R. Matear, 2007: Role of the Southern Annular Mode (SAM) in Southern Ocean
740 CO₂ uptake. *Glob. Biogeochem. Cycles*, **21**, GB2016 PB–, doi:10.1029/2006GB002714.
- 741 Liu, L., and R. Huang, 2012: The global subduction/obduction rates: Their interannual and
742 decadal variability. *Journal of Climate*, **25**, 1096–1115, doi:10.1175/2011JCLI4228.1.
- 743 Losch, M., D. Menemenlis, J.-M. Campin, P. Heimbach, and C. Hill, 2010: On the formulation
744 of sea-ice models. Part 1: Effects of different solver implementations and parameterizations.
745 *Ocean Modelling*, **33** (1-2), 129–144, doi:10.1016/j.ocemod.2009.12.008.
- 746 Lovenduski, N., and T. Ito, 2009: The future evolution of the Southern Ocean CO₂ sink. *Journal*
747 *of Marine Research*, **67**, 597–617.
- 748 Lumpkin, R., and K. Speer, 2007: Global ocean meridional overturning. *Journal of Physical*
749 *Oceanography*, **37**, 2550–2562, doi:10.1175/JPO3130.1.

- 750 Luyten, J., J. Pedlosky, and H. Stommel, 1983: The ventilated thermocline. *Journal of Physical*
751 *Oceanography*, **13** (2), 292–309.
- 752 Marotzke, J., R. Giering, K. Zhang, D. Stammer, C. Hill, and T. Lee, 1999a: Construction of
753 the Adjoint MIT Ocean General Circulation Model and Application to Atlantic Heat Transport
754 Sensitivity. *MIT report*, 1–50.
- 755 Marotzke, J., R. Giering, K. Q. Zhang, D. Stammer, C. Hill, and T. Lee, 1999b: Construction
756 of the adjoint MIT ocean general circulation model and application to Atlantic heat transport
757 sensitivity. *Journal of Geophysical Research: Atmospheres*, **104** (C12), 29 529–29 547, doi:
758 10.1029/1999JC900236.
- 759 Marshall, J., and K. Speer, 2012: Closure of the meridional overturning circulation through South-
760 ern Ocean upwelling. *Nature Geoscience*, **5**, 171–180, doi:10.1038/ngeo1391.
- 761 Mazloff, M., P. Heimbach, and C. Wunsch, 2010: An Eddy-Permitting Southern Ocean State
762 Estimate. *Journal of Physical Oceanography*, **40**, 880–899.
- 763 McAufield, E. K., 2019: Lagrangian study of the Southern Ocean circulation. Ph.D. thesis, Uni-
764 versity of Cambridge, URL <https://doi.org/10.17863/CAM.36004>.
- 765 McDougall, T., and P. Barker, 2011: Getting started with TEOS-10 and the Gibbs Seawater (GSW)
766 Oceanographic Toolbox. *SCOR/IAPSO WG127*.
- 767 Meijers, A. J. S., 2013: The Southern Ocean in CMIP5. *Proceedings of the Royal Society A*, 1–21.
- 768 Meijers, A. J. S., I. Cerovečki, B. A. King, and V. Tamsitt, 2019: A See-Saw in Pacific Sub-
769 antarctic Mode Water Formation Driven by Atmospheric Modes. *Geophysical Research Letters*,
770 2019GL085280, doi:10.1029/2019GL085280, URL [https://onlinelibrary.wiley.com/doi/abs/10.](https://onlinelibrary.wiley.com/doi/abs/10.1029/2019GL085280)
771 1029/2019GL085280.

772 Morrison, A., A. Hogg, and M. L. Ward, 2011: Sensitivity of the Southern Ocean overturning
773 circulation to surface buoyancy forcing. *Geophysical Research Letters*, **38** (L14602), doi:10.
774 1029/2011GL048031.

775 Musgrave, D., 1990: Numerical studies of tritium and helium-3 in the thermocline. *Journal of*
776 *Physical Oceanography*, **20**, 344–373.

777 Primeau, F., and M. Holzer, 2006: The Ocean’s Memory of the Atmosphere: Residence-Time
778 and Ventilation-Rate Distributions of Water Masses. *Journal of Physical Oceanography*, **36**,
779 1439–1456.

780 Roemmich, D., J. Church, J. Gilson, D. Monselesan, P. Sutton, and S. Wijffels, 2015: Unabated
781 planetary warming and its ocean structure since 2006. *Nature Publishing Group*, **5** (3), 240,
782 doi:10.1038/nclimate2513.

783 Russell, J., K. Dixon, A. Gnanadesikan, R. Stouffer, and J. Toggweiler, 2006: The Southern Hemi-
784 sphere westerlies in a warming world: Propping open the door to the deep ocean. *Journal of*
785 *Climate*, **19**, 6382–6390.

786 Sabine, C., and Coauthors, 2004: The oceanic sink for anthropogenic CO₂. *Science*, **305** (367),
787 doi:10.1126/science.1097403.

788 Sallée, J., and S. Rintoul, 2011: Parameterization of eddy-induced subduction in the Southern
789 Ocean surface-layer. *Ocean Modelling*, **39**, 146–153.

790 Sallée, J., K. Speer, S. Rintoul, and S. Wijffels, 2010a: Southern Ocean thermocline ventilation.
791 *Journal of Physical Oceanography*, **40**, 509–529.

792 Sallée, J.-B., R. J. Matear, S. R. Rintoul, and A. Lenton, 2012: Localized subduction of anthro-
793 pogenic carbon dioxide in the Southern Hemisphere oceans. *Nature Geoscience*, **5** (8), 579–584,
794 doi:10.1038/ngeo1523.

795 Sallée, J.-B., K. Speer, S. Rintoul, and S. Wijffels, 2010b: Southern Ocean Thermocline Ventila-
796 tion. *Journal of Physical Oceanography*, **40** (3), 509–529, doi:10.1175/2009jpo4291.1.

797 Sarmiento, J. L., N. Gruber, M. A. Brzezinski, and J. P. Dunne, 2004: High-latitude controls
798 of thermocline nutrients and low latitude biological productivity. *Nature*, **427** (6969), 56–60,
799 doi:10.1038/nature02127.

800 Schmidtko, S., and G. C. Johnson, 2012: Multidecadal Warming and Shoaling of Antarctic Inter-
801 mediate Water*. *Journal of Climate*, **25** (1), 207–221, doi:10.1175/JCLI-D-11-00021.1, URL
802 <http://journals.ametsoc.org/doi/abs/10.1175/JCLI-D-11-00021.1>.

803 Sévellec, F., and A. V. Fedorov, 2015: Optimal excitation of AMOC decadal variability: Links to
804 the subpolar ocean. *Progress in Oceanography*, **132**, 287–304, doi:10.1016/j.pocean.2014.02.
805 006.

806 Speer, K., and G. Forget, 2013: Global Distribution and Formation of Mode Waters. *Ocean*
807 *Circulation and Climate - A 21st Century Perspective*, Elsevier, 211–226, doi:10.1016/
808 B978-0-12-391851-2.00009-X.

809 Speer, K., S. Rintoul, and B. Sloyan, 2000: The Diabatic Deacon Cell. *Journal of Physical*
810 *Oceanography*, **30** (12), 3212–3222.

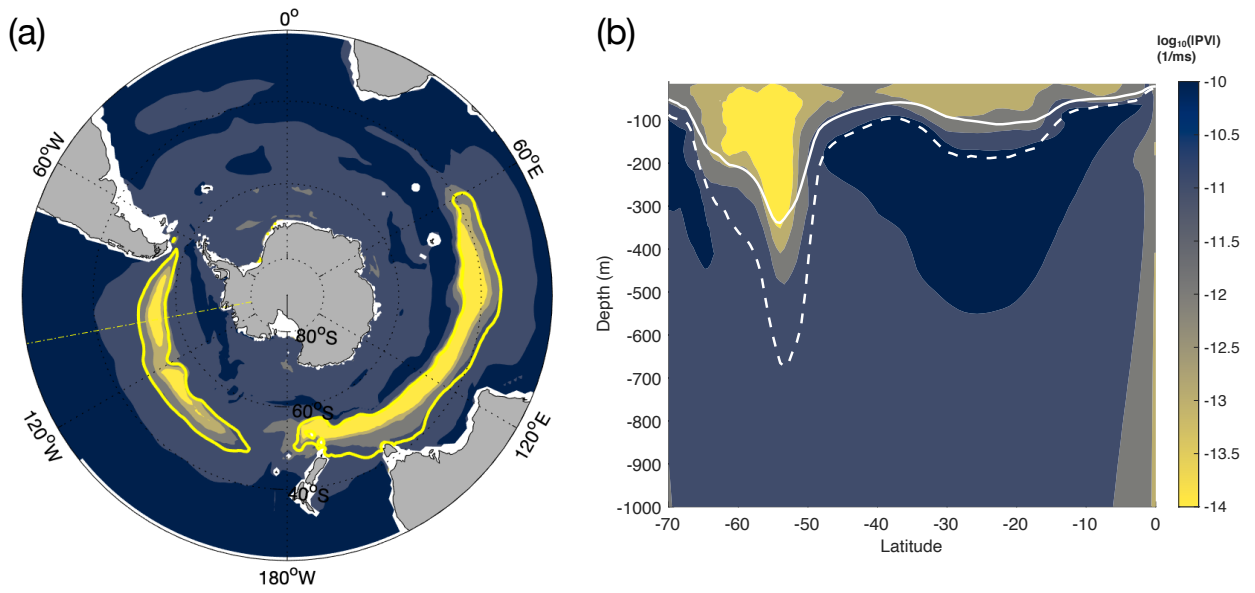
811 Speer, K., and E. Tziperman, 1992: Rates of water mass formation in the North Atlantic Ocean.
812 *Journal of Physical Oceanography*, **22**, 93–104.

- 813 Talley, L., 2008: Freshwater transport estimates and the global overturning circulation: Shallow,
814 deep and throughflow components. *Progress in Oceanography*, **78** (3), 257–303, doi:10.1016/j.
815 pocean.2008.05.001.
- 816 Talley, L., 2013: Closure of the Global Overturning Circulation Through the Indian, Pa-
817 cific, and Southern Oceans: Schematics and Transports. *Oceanography*, **26** (1), 80–97, doi:
818 10.5670/oceanog.2013.07.
- 819 Thacker, W. C., and R. B. Long, 1988: Fitting dynamics to data. *Journal of Geophysical Research*,
820 **93** (C2), 1227–1240, doi:10.1029/JC093iC02p01227.
- 821 Thompson, A. F., and J.-B. Sallée, 2012: Jets and Topography: Jet Transitions and the Impact
822 on Transport in the Antarctic Circumpolar Current. *Journal of Physical Oceanography*, **42** (6),
823 956–972, doi:10.1175/JPO-D-11-0135.1.
- 824 Trossman, D. S., L. Thompson, S. Mecking, and M. J. Warner, 2012: On the formation, ventilation,
825 and erosion of mode waters in the North Atlantic and Southern Oceans. *Journal of Geophysical*
826 *Research - Oceans*, **117**, doi:10.1029/2012JC008090.
- 827 Verdy, A., M. R. Mazloff, B. D. Cornuelle, and S. Y. Kim, 2014: Wind-Driven Sea Level Variabil-
828 ity on the California Coast: An Adjoint Sensitivity Analysis. *Journal of Physical Oceanography*,
829 **44** (1), 297–318, doi:10.1175/JPO-D-13-018.1.

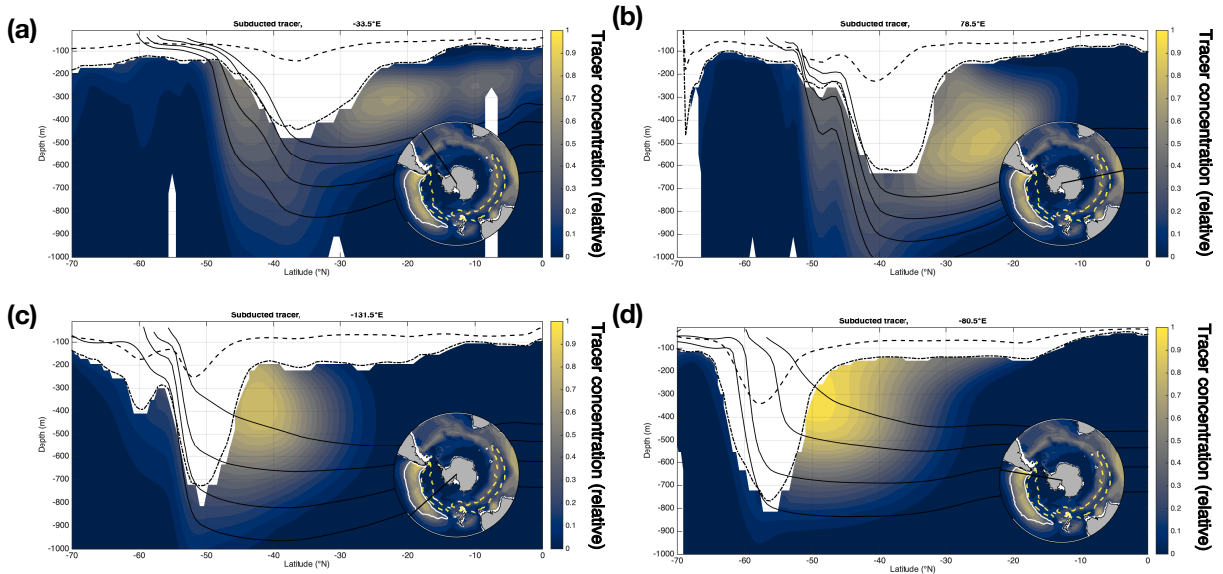
830 **LIST OF FIGURES**

- 831 **Fig. 1.** Southern Ocean potential vorticity and mixed layer depth. Shown are median values of
832 annual minimum $\log_{10}(|PV|)$ across the years 1992-2011 as (a) a section through $z=300$ m.
833 The yellow contour indicates a section through the median mixed layer mask at $z=300$ m
834 depth, and the yellow dot-dash line indicates the location of the section in panel (b). (b)
835 Section of median values of annual minimum $\log_{10}(|PV|)$ across the years 1992-2011 at
836 $100.5^\circ W$, with ensemble median values for the annual mean (solid white line) and ASO
837 mean (dashed white line) mixed layer depths. PV has units of $1/ms$ 41
- 838 **Fig. 2.** Defining the recently ventilated subsurface. Shading indicates the ensemble mean, annual
839 mean tracer after 10 years of transport. Values have been normalized by the maximum value.
840 Also shown is the mean mixed layer depth (dashed lines) and maximum mixed layer depth
841 (dash-dot lines) over the length of the 10 year simulation. Solid lines indicate potential
842 density surfaces ($\sigma_0 = 26.9 \text{ kg m}^{-3}$ to $\sigma_0 = 27.2 \text{ kg m}^{-3}$, spaced every 0.1 kg m^{-3}). Tracer
843 above the maximum mixed layer has been discarded. Although we discard the tracer lighter
844 than $\sigma_0 = 26.9 \text{ kg m}^{-3}$ when defining the RVP, we kept this tracer in the figure for visual-
845 ization purposes. Inset figures are column-integrated tracer histogram, which is normalized
846 by the maximum column-integrated value, after discarding the tracer above the maximum
847 mixed layer, along with a section through the ensemble median mixed layer mask at $z=300$
848 depth (yellow dashed contours) and a section through the ensemble median ventilated water
849 mask at $z=553$ m (white solid contour). Sections are shown for (a) $33.5^\circ W$, (b) $78.5^\circ E$, (c)
850 $131.5^\circ W$, and (d) $80.5^\circ W$ 42
- 851 **Fig. 3.** Vertical structure of the ensemble median RVP. Yellow regions are included in the RVP.
852 A section through the ensemble median mixed layer mask at roughly 300 m is shown for
853 reference (white solid contours). 43
- 854 **Fig. 4.** (a)-(f) Interannual variability in the RVP expressed as column-integrated volume in units of
855 10^{12} m^3 . The years listed in the titles indicate the dates of the tracer transport (i.e. released
856 1 Jan 1996 and transported until 31 Dec 2006). Percentages in the top left of each panel
857 indicate volume changes relative to the 1996-2006 experiment. (g) Comparison of ventilated
858 volume by depth level across release years. We used these tracer distributions to define the
859 RVP in a self-consistent way; in this work, we do not examine the causes for the variation
860 in RVP. 44
- 861 **Fig. 5.** Relative ensemble mean sensitivities of RVP to density-compensated temperature anoma-
862 lies (i.e. kinematic sensitivities). Also shown is a section through the RVP at roughly 553
863 m depth (black solid line), a section through the mixed layer mask at roughly 300 m depth
864 (green dashed line), a depth contour (red solid line; 95 m for the left column, 552 m for the
865 right column), and the SAF proxy (magenta solid line). All fields have been scaled by the
866 grid cell thickness Δz to allow for comparison between different depth levels. The plots have
867 been further scaled by the global maximum sensitivity for the entire adjoint run to allow for
868 comparison between different lags. 45
- 869 **Fig. 6.** Kinematic RMS sensitivities averaged over different volumes, indicating propagation
870 timescales and relative magnitudes. Timescale increases from right to left, as indicated
871 by more negative lags (i.e. longer lead times). Lines indicate ensemble means, and shad-
872 ing indicates one standard deviation across the ensemble. All values have been scaled by
873 the same maximum of $0.0017 \text{ }^\circ C/^\circ C$ and can be compared relative to each other. We show
874 (a) the global mean sensitivity, (b) within the control volume (RVP) or not, (c) inside or
875 outside of the 300 m MLD mask, (d), north or south of the SAF proxy, (e) in the upper
876 100 m in different basins, and (e) below 100 m in different basins. Note that the axes in

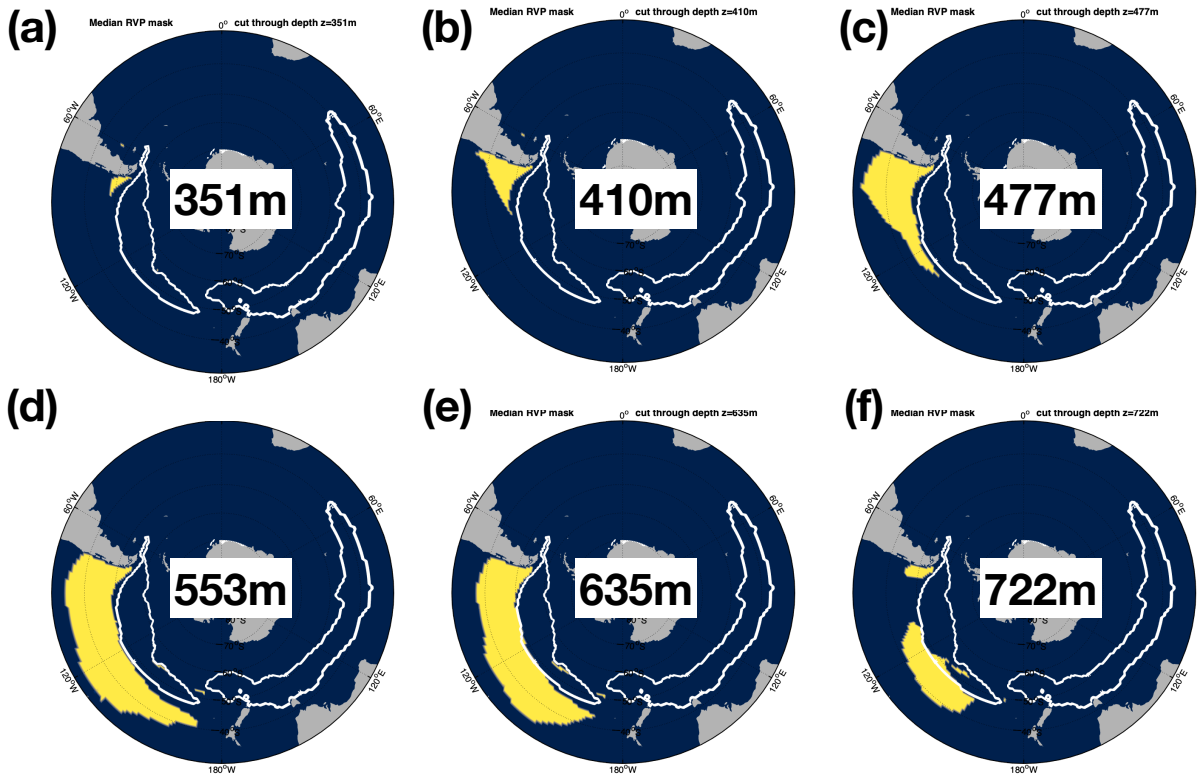
877	panel (e) differ from the others. To define the basins, we used the standard ECCOv4 masks	
878	that are part of the gcmfaces package (see acknowledgements), and we chose 120°W as	
879	the dividing longitude between the East and West Pacific basins. South of 30°S, the basins	
880	are roughly demarcated by longitude: Atlantic (70°W-20°E), Indian (20°E-150°E), Western	
881	Pacific (150°E-120°W), and Eastern Pacific (120°W-70°W).	46
882	Fig. 7. Relative ensemble mean sensitivities to changes in density (i.e. dynamic sensitivities). Scal-	
883	ing and units are the same as in Figure 5.	47
884	Fig. 8. RMS dynamic sensitivity time series. The panels and scaling are identical to those in Figure	
885	6. Timescale increases from right to left.	48
886	Fig. 9. Schematic illustrating the main kinematic and dynamic sensitivities up to approximately 10	
887	years lag. Chalk lines with arrows indicate kinematic sensitivities, with the vertical structure	
888	indicated by color. Weaker pathways by dashed lines. The circles connected by lines indicate	
889	where dynamic sensitivities resemble dipoles. Hot-spots are defined as regions that are either	
890	perennially sensitive or regions that feature a large seasonal amplitude throughout the 10-	
891	year timescale of the schematic. The reference contours include the RVP at 553 m (thick	
892	solid black line), the mixed layer mask at roughly 300 m depth (green dashed line), the SAF	
893	proxy (magenta solid line), and the 3000 m depth contour (thin gray lines).	49



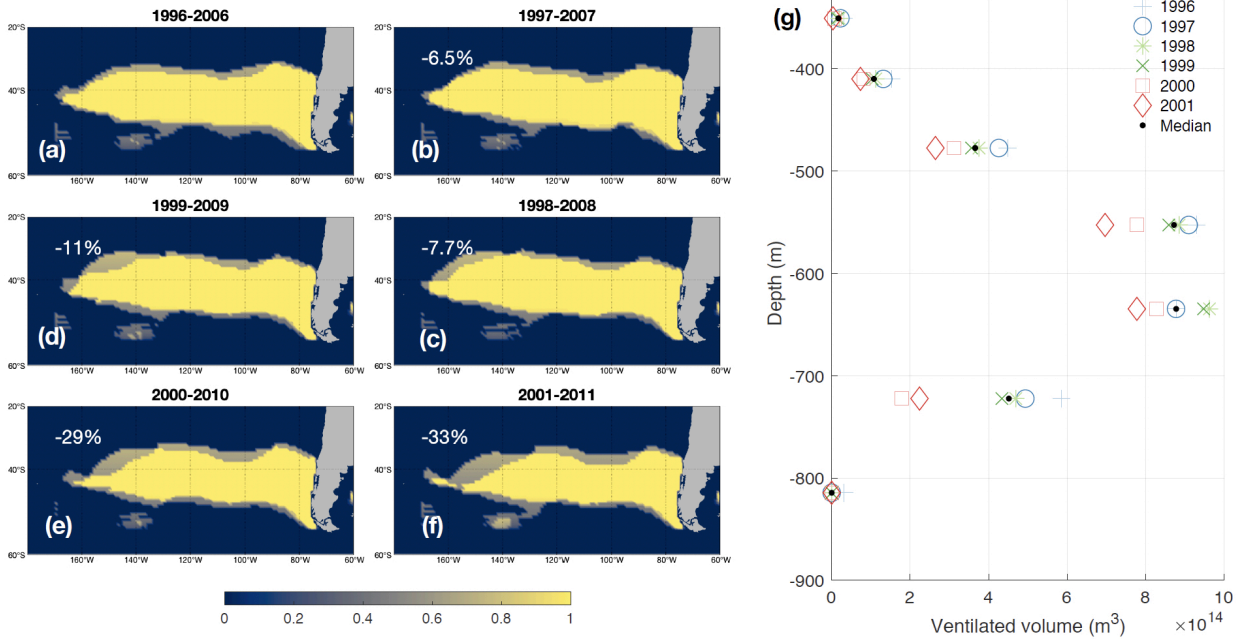
894 FIG. 1. Southern Ocean potential vorticity and mixed layer depth. Shown are median values of annual min-
 895 imum $\log_{10}(|PV|)$ across the years 1992-2011 as (a) a section through $z=300$ m. The yellow contour indicates
 896 a section through the median mixed layer mask at $z=300$ m depth, and the yellow dot-dash line indicates the
 897 location of the section in panel (b). (b) Section of median values of annual minimum $\log_{10}(|PV|)$ across the
 898 years 1992-2011 at $100.5^\circ W$, with ensemble median values for the annual mean (solid white line) and ASO
 899 mean (dashed white line) mixed layer depths. PV has units of $1/ms$.



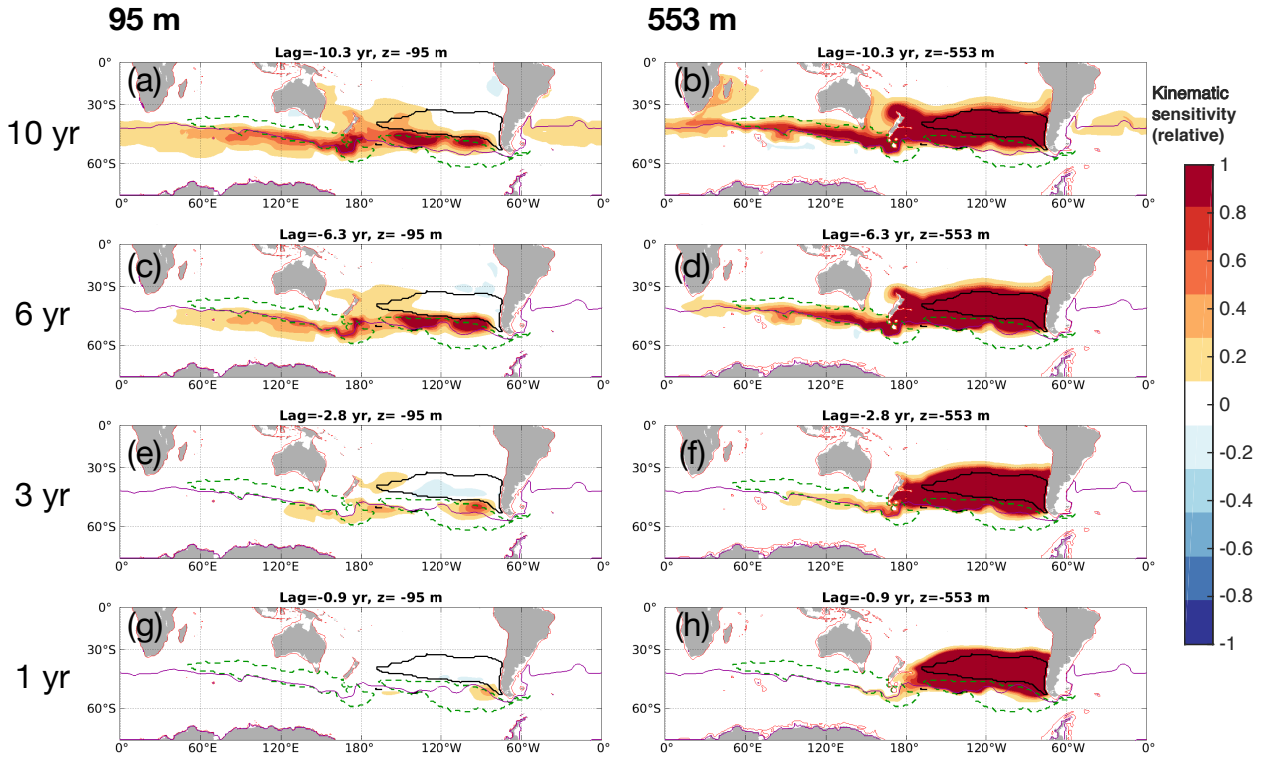
900 FIG. 2. Defining the recently ventilated subsurface. Shading indicates the ensemble mean, annual mean tracer
 901 after 10 years of transport. Values have been normalized by the maximum value. Also shown is the mean
 902 mixed layer depth (dashed lines) and maximum mixed layer depth (dash-dot lines) over the length of the 10
 903 year simulation. Solid lines indicate potential density surfaces ($\sigma_0 = 26.9 \text{ kg m}^{-3}$ to $\sigma_0 = 27.2 \text{ kg m}^{-3}$, spaced
 904 every 0.1 kg m^{-3}). Tracer above the maximum mixed layer has been discarded. Although we discard the tracer
 905 lighter than $\sigma_0 = 26.9 \text{ kg m}^{-3}$ when defining the RVP, we kept this tracer in the figure for visualization purposes.
 906 Inset figures are column-integrated tracer histogram, which is normalized by the maximum column-integrated
 907 value, after discarding the tracer above the maximum mixed layer, along with a section through the ensemble
 908 median mixed layer mask at $z=300$ depth (yellow dashed contours) and a section through the ensemble median
 909 ventilated water mask at $z=553$ m (white solid contour). Sections are shown for (a) 33.5°W , (b) 78.5°E , (c)
 910 131.5°W , and (d) 80.5°W .



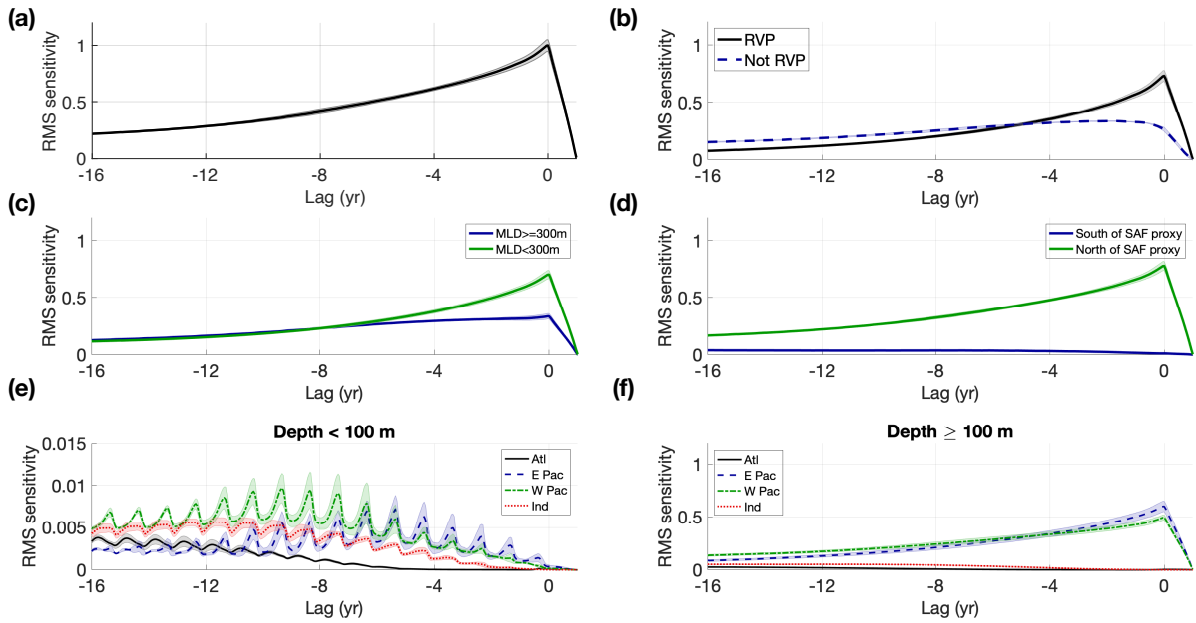
911 FIG. 3. Vertical structure of the ensemble median RVP. Yellow regions are included in the RVP. A section
 912 through the ensemble median mixed layer mask at roughly 300 m is shown for reference (white solid contours).



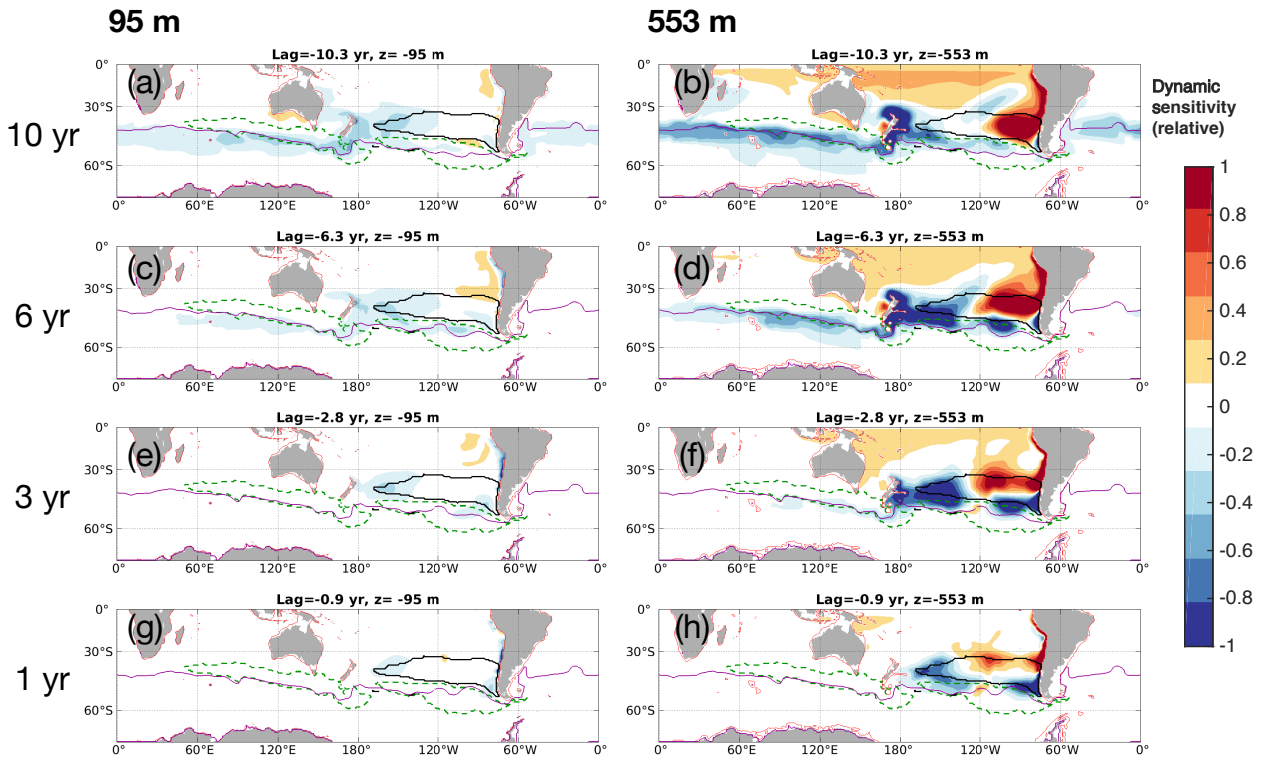
913 FIG. 4. (a)-(f) Interannual variability in the RVP expressed as column-integrated volume in units of 10^{12} m^3 .
 914 The years listed in the titles indicate the dates of the tracer transport (i.e. released 1 Jan 1996 and transported
 915 until 31 Dec 2006). Percentages in the top left of each panel indicate volume changes relative to the 1996-2006
 916 experiment. (g) Comparison of ventilated volume by depth level across release years. We used these tracer
 917 distributions to define the RVP in a self-consistent way; in this work, we do not examine the causes for the
 918 variation in RVP.



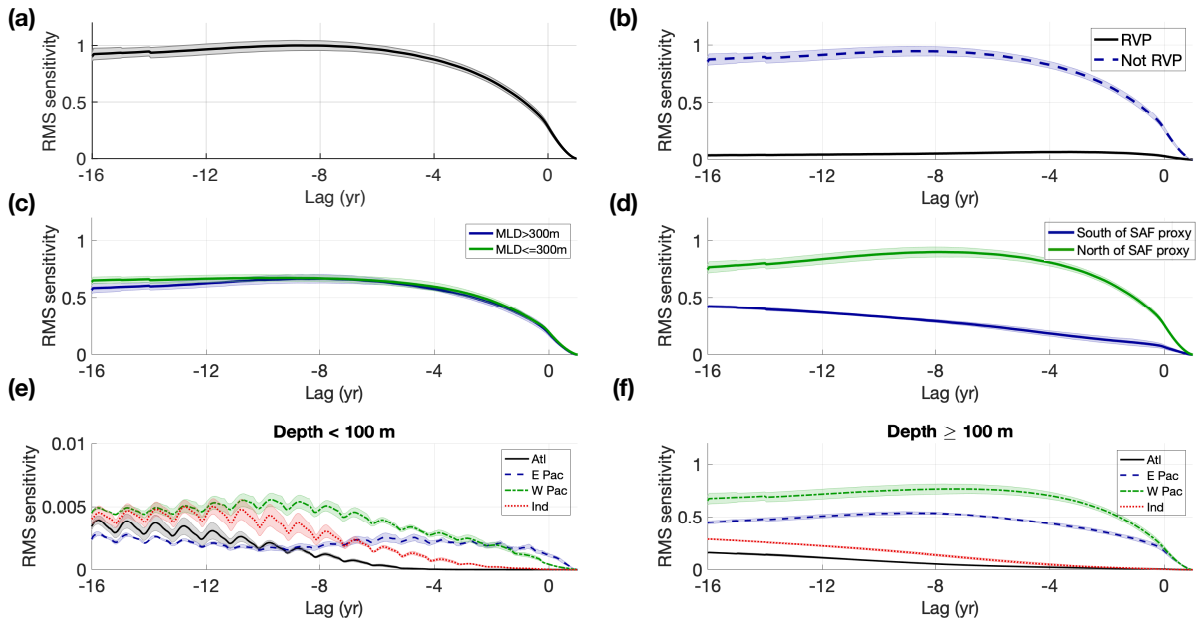
919 FIG. 5. Relative ensemble mean sensitivities of RVP to density-compensated temperature anomalies (i.e.
 920 kinematic sensitivities). Also shown is a section through the RVP at roughly 553 m depth (black solid line), a
 921 section through the mixed layer mask at roughly 300 m depth (green dashed line), a depth contour (red solid
 922 line; 95 m for the left column, 552 m for the right column), and the SAF proxy (magenta solid line). All fields
 923 have been scaled by the grid cell thickness Δz to allow for comparison between different depth levels. The plots
 924 have been further scaled by the global maximum sensitivity for the entire adjoint run to allow for comparison
 925 between different lags.



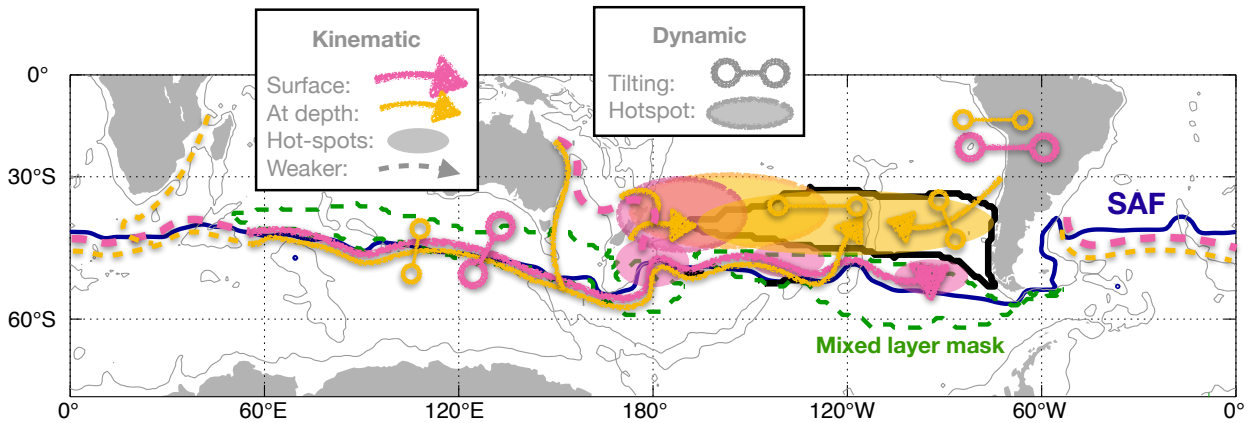
926 FIG. 6. Kinematic RMS sensitivities averaged over different volumes, indicating propagation timescales and
 927 relative magnitudes. Timescale increases from right to left, as indicated by more negative lags (i.e. longer lead
 928 times). Lines indicate ensemble means, and shading indicates one standard deviation across the ensemble. All
 929 values have been scaled by the same maximum of $0.0017\text{ }^{\circ}\text{C}/^{\circ}\text{C}$ and can be compared relative to each other. We
 930 show (a) the global mean sensitivity, (b) within the control volume (RVP) or not, (c) inside or outside of the 300
 931 m MLD mask, (d), north or south of the SAF proxy, (e) in the upper 100 m in different basins, and (e) below
 932 100 m in different basins. Note that the axes in panel (e) differ from the others. To define the basins, we used the
 933 standard ECCOV4 masks that are part of the gcmfaces package (see acknowledgements), and we chose 120°W
 934 as the dividing longitude between the East and West Pacific basins. South of 30°S , the basins are roughly
 935 demarcated by longitude: Atlantic (70°W - 20°E), Indian (20°E - 150°E), Western Pacific (150°E - 120°W), and
 936 Eastern Pacific (120°W - 70°W).



937 FIG. 7. Relative ensemble mean sensitivities to changes in density (i.e. dynamic sensitivities). Scaling and
 938 units are the same as in Figure 5.



939 FIG. 8. RMS dynamic sensitivity time series. The panels and scaling are identical to those in Figure 6.
 940 Timescale increases from right to left.



941 FIG. 9. Schematic illustrating the main kinematic and dynamic sensitivities up to approximately 10 years lag.
 942 Chalk lines with arrows indicate kinematic sensitivities, with the vertical structure indicated by color. Weaker
 943 pathways by dashed lines. The circles connected by lines indicate where dynamic sensitivities resemble dipoles.
 944 Hot-spots are defined as regions that are either perennially sensitive or regions that feature a large seasonal
 945 amplitude throughout the 10-year timescale of the schematic. The reference contours include the RVP at 553
 946 m (thick solid black line), the mixed layer mask at roughly 300 m depth (green dashed line), the SAF proxy
 947 (magenta solid line), and the 3000 m depth contour (thin gray lines).